

₁ A novel inf–sup–based volumetric constraint ratio and
₂ its implementation via mixed FE-meshfree formulation

₃ Junchao Wu^{a,*}, Yingjie Chu^b, Yangtao Xu^a

^a Key Laboratory for Intelligent Infrastructure and Monitoring of Fujian Province, College
of Civil Engineering, Huaqiao University , Xiamen, Fujian, 361021, China

^b Fujian Key Laboratory of Digital Simulations for Coastal Civil Engineering, Department
of Civil Engineering, Xiamen University , Xiamen, Fujian, 361005, China

₄ **Abstract**

Numerical formulations for incompressible materials often suffer from volumetric locking, which reduces the accuracy of displacement solutions and introduces oscillations in the pressure field. A well-chosen constraint ratio can mitigate this issue, but traditional approaches lack a theoretical foundation based on the inf–sup (or LBB) condition, which is essential for the stability of mixed formulations. This paper introduces a novel optimal constraint ratio derived from the inf–sup condition to address volumetric locking. The inf–sup test, a numerical tool for verifying the inf–sup condition, is reaffirmed to be equivalent to the inf–sup condition through a variational approach. By incorporating a complete polynomial space whose dimension matches the number of displacement degrees of freedom (DOFs), a new inf–sup value estimator is developed, explicitly considering the constraint ratio. For a given number of displacement DOFs, when the pressure DOFs of a numerical formulation remain below a stabilized number that falls into the optimal constraint ratio range, this numerical formulation actually satisfies the inf–sup condition. To implement the optimal constraint ratio, a mixed finite element and meshfree formulation is proposed, where displacements are discretized using traditional finite element approximations, and pressures are approximated via the reproducing kernel meshfree method. Leveraging the globally smooth reproducing kernel shape functions, the constraint ratio can be flexibly adjusted to meet the inf–sup condition without the limit of element. For computational efficiency and ease of implementation, pressure nodes are placed on selected displacement nodes to maintain the optimal constraint ratio. Inf–sup tests and a series of 2D and 3D incompressible elasticity examples validate the proposed constraint ratio, demonstrating its effectiveness in eliminating volumetric locking and enhancing the performance of mixed finite element and meshfree formulations.

₅ **Keywords:** Optimal constraint ratio, Inf–sup condition estimator, Volumetric
₆ locking, Mixed formulation, Reproducing kernel meshfree approximation

*Corresponding author

Email address: jcwu@hqu.edu.cn (Junchao Wu)

7 **1. Introduction**

8 The volumetric constraint is a necessary condition in the numerical formulation
 9 of incompressible materials like rubber and hydrogel. Proper imposition of
 10 this constraint is crucial for obtaining better numerical solutions; insufficient or
 11 excessive constraints will reduce the accuracy and stability of the solution [1].
 12 The volumetric constraint ratio [2], denoted as r , is often used to measure the
 13 level of constraint. It is defined as the total degrees of freedom (DOFs) of dis-
 14 placement divided by the total DOFs of pressure. Ideally, the optimal constraint
 15 ratio should be consistent with its governing partial differential equations. For
 16 example, in the two-dimensional (2D) case, the optimal constraint ratio is 2,
 17 since there are two governing equations for displacement and one for pressure.
 18 When the constraint ratio is less than 2, the formulation suffers from volumetric
 19 locking, while a constraint ratio greater than 2 can cause a coarse solution for
 20 pressure. These observations have been summarized as follows[2]:

$$r = \frac{2n_u}{n_p}, \quad \begin{cases} r > 2 & \text{too few constraints} \\ r = 2 & \text{optimal} \\ r < 2 & \text{too many constraints} \\ r \leq 1 & \text{severe locking} \end{cases} \quad (1)$$

21 where n_u and n_p are the numbers of control nodes for displacement and pressure,
 22 respectively. Classifying the locked status via the constraint ratio is straight-
 23 forward but imprecise. For instance, the constraint ratio can remain 2 while
 24 the pressure is discretized using continuous shape functions identical to the
 25 displacement's approximation. However, volumetric locking still exists in this
 26 formulation [2].

27 The inf-sup condition, also known as the Ladyzhenskay–Babuka–Brezzi
 28 (LBB) condition [3, 4], is a more precise requirement for a locking-free for-
 29 mulation. This condition is based on the mixed formulation framework, and
 30 when the inf-sup condition is satisfied, both the accuracy and stability of the
 31 mixed-formulation can be ensured. However, verifying the inf-sup condition is
 32 non-trivial. An eigenvalue problem namely inf-sup test can be used to check
 33 this condition numerically [5, 6, 7, 8]. Analytically, Brezzi and Fortin proposed
 34 a two-level projection framework that always satisfies the inf-sup condition, al-
 35 lowing it to be checked by identifying whether the formulation is included in
 36 this framework. Both analytical and numerical methods to check the inf-sup
 37 condition are complex, and the relationship between the constraint ratio and
 38 the inf-sup condition remains unclear.

39 To address volumetric constraint issues, adjusting the constraint ratio to an
 40 appropriate level is commonly used and easily implemented. In traditional finite
 41 element methods (FEM), this adjustment is carried out based on elements since
 42 the DOFs are embedded in each element. Conventional FEM often exhibits
 43 an over-constrained status. Reducing the approximation order of pressure in
 44 mixed formulation can alleviate the constraint burden, such as with the well-
 45 known Q4P1 (4-node quadrilateral displacement element with 1-node piecewise

constant pressure element) and Q8P3. Globally, using continuous shape functions to link the local pressure DOFs in each element can also reduce the total number of pressure DOFs and increase the constraint ratio, such as with T6C3 (6-node triangular displacement element with 3-node continuous linear pressure element) and Q9C4 (Taylor–Hood element) [9]. These schemes belong to the mixed formulation framework and can also be implemented through a projection approach, where the pressure approximant is projected into a lower-dimensional space. Examples include selective integration methods [10, 11], B–bar or F–bar methods [12, 13, 14, 15], pressure projection methods [16, 17, 18, 19, 20], and enhanced strain method [21]. Meanwhile, conventional 3-node triangular elements arranged in a regular cross pattern can also reduce the dimension of the pressure space [22]. It should be noted that not all of these methods meet the inf–sup condition despite alleviating volumetric locking and producing a good displacement solution. Some methods, like Q4P1, show significant oscillation for the pressure solution, known as spurious pressure mode or checkerboard mode [22]. In such cases, additional stabilization approaches, such as variational multi-scale stabilization (VMS) [23, 24, 25, 26, 27], Galerkin/least-squares (GLS) [28], or Streamline upwind/Petrov–Galerkin formulation (SUPG) [29, 30] are required to eliminate the oscillations in pressure.

Another class of FEM methods adjusts the constraint ratio by increasing the displacement DOFs. For instance, based on 3-node triangular elements, Arnold et al. [31, 32] used a cubic bubble function in each element to increase the displacement DOFs, known as the MINI element. It has been shown that this method belongs to the VMS framework [33], and its fulfillment of the inf–sup condition can be analytically evidenced using the two-level projection framework [7]. The Crouzeix–Raviart element [34] transfers the DOFs from the triangular vertices to edges, increasing the constraint ratio since, for triangular topology, the number of edges is greater than that of vertices. More details about FEM technology for volumetric constraint issues can be found in Refs. [2, 4, 35].

In the past two decades, various novel approximations equipped with globally smooth shape functions, such as moving least-squares approximation [36], reproducing kernel approximation [37, 38], radial basis functions [39, 40], maximum-entropy approximation [41], and NURBS approximation [42, 43], have been proposed. In these approaches, the approximant pressure evaluated by the derivatives of globally continuous shape functions also maintains a constraint ratio of 2 in 2D incompressible elasticity problems. However, the corresponding results still show lower accuracy caused by locking [44, 45]. Widely-used locking-free technologies for FEM are introduced in these approaches to enhance their performance. For example, Moutsanidis et al. [46, 47] employed selective integration and B–bar, F–bar methods for reproducing kernel particle methods. Wang et al. [48] applied selective integration schemes with bubble-stabilized functions to node-based smoothed particle FEM. Elguedj et al. [49] proposed the B–bar and F–bar NURBS formulations for linear and nonlinear incompressible elasticity. Chen et al. [50] adopted the pressure projection approach for reproducing kernel formulations for nearly-incompressible problems, which was later extended

to Stokes flow formulations by Goh et al. [51]. Bombarde et al. [52] developed a block-wise NURBS formulation for shell structures, eliminating locking via pressure projection. Casquero and Golestanian [53] proposed a NURBS-based continuous-assumed-strain element to alleviate volumetric locking. Most of these approximations offer better flexibility for arranging DOFs since their shape function constructions are no longer element-dependent. Huerta et al.[54] proposed a reproducing kernel approximation with divergence-free basis functions to avoid volumetric strain entirely , although this approach is unsuitable for compressible cases. Wu et al. [55] added extra displacement DOFs in FEM elements to resolve the locking issue, constructing local shape functions using generalized meshfree interpolation to maintain consistency. Vu-Huu et al. [56] employed different-order polygonal finite element shape functions to approximate displacement and pressure, embedding a bubble function in each element for stabilization.

This work proposes a more precise optimal volumetric constraint ratio and implements a locking-free mixed FE-meshfree formulation with this optimal constraint ratio. Firstly, the inf-sup condition is derived in a new form, showing that the inf-sup value equals to the lowest non-zero eigenvalue of dilatation stiffness in the context of variational analysis. Subsequently, involving a complete polynomial space with dimensions identical to displacement DOFs, the number of non-zero eigenvalues can be analytically calculated, and a new estimator considering the constraint ratio is established. From this estimator, the optimal constraint ratio is defined with a stabilized number of pressure nodes. If the constraint ratio exceeds the locking ratio, the formulation will show severe locking. When the constraint ratio is lower than the optimal ratio, the formulation achieves satisfactory results, and the inf-sup condition is fulfilled. This estimator provides a strong link between the inf-sup value and the pressure DOFs, making it possible to justify the locking status by counting the pressure nodes. Furthermore, a mixed FE-meshfree formulation is proposed to verify the optimal constraint ratio. In this mixed formulation, the displacement is approximated by traditional finite element methods, and the pressure is discretized by reproducing kernel meshfree approximation. With the aid of global RK shape functions, the pressure's DOFs can be adjusted arbitrarily without considering approximation order and numerical integration issues to maintaining the constraint ratio as optimal.

The remainder of this paper is organized as follows: Section 2 reviews the mixed formulation framework for incompressible elasticity problems. In Section 3, a novel estimator of the inf-sup value is developed, from which the optimal constraint ratio is obtained. Section 4 introduces the mixed FE-meshfree formulation and its corresponding nodal distribution schemes. Section 5 verifies the proposed optimal constraint ratio using a set of benchmark incompressible elasticity examples, studying error convergence and stability property for the mixed FE-meshfree approximation. Finally, the conclusions are presented in Section 6.

¹³⁶ **2. Mixed-formulation**

¹³⁷ *2.1. Nearly-incompressible elasticity*

¹³⁸ Consider a body $\Omega \in \mathbb{R}^{n_d}$ with boundary Γ in n_d -dimension, where Γ_t and
¹³⁹ Γ_g denote its natural boundary and essential boundary, respectively, such that
¹⁴⁰ $\Gamma_t \cup \Gamma_g = \Gamma$, $\Gamma_t \cap \Gamma_g = \emptyset$. The corresponding governing equations for the mixed
¹⁴¹ formulation are given by:

$$\begin{cases} \nabla \cdot \boldsymbol{\sigma} + \mathbf{b} = \mathbf{0} & \text{in } \Omega \\ \frac{p}{\kappa} + \nabla \cdot \mathbf{u} = 0 & \text{in } \Omega \\ \boldsymbol{\sigma} \cdot \mathbf{n} = \mathbf{t} & \text{on } \Gamma_t \\ \mathbf{u} = \mathbf{g} & \text{on } \Gamma_g \end{cases} \quad (2)$$

¹⁴² where \mathbf{b} denotes the prescribed body force in Ω . \mathbf{t}, \mathbf{g} are prescribed traction and
¹⁴³ displacement on natural and essential boundaries, respectively. \mathbf{u} and p , standing
¹⁴⁴ for displacement and hydrostatic pressure, respectively, are the variables of
¹⁴⁵ this problem. ∇ is the gradient tensor defined by $\nabla = \frac{\partial}{\partial x_i} \mathbf{e}_i$. $\boldsymbol{\sigma}$ denotes the
¹⁴⁶ stress tensor and has the following form:

$$\boldsymbol{\sigma}(\mathbf{u}, p) = p \mathbf{1} + 2\mu \nabla^d \mathbf{u} \quad (3)$$

¹⁴⁷ in which $\mathbf{1} = \delta_{ij} \mathbf{e}_i \otimes \mathbf{e}_j$ is the second-order identity tensor. $\nabla^d \mathbf{u}$ is the deviatoric
¹⁴⁸ gradient of \mathbf{u} and can be evaluated by:

$$\nabla^d \mathbf{u} = \frac{1}{2} (\mathbf{u} \nabla + \nabla \mathbf{u}) - \left(\frac{1}{3} \nabla \cdot \mathbf{u} \right) \mathbf{1} \quad (4)$$

¹⁴⁹ and κ, μ are the bulk modulus and shear modulus, respectively, and they can
¹⁵⁰ be represented by Young's modulus E and Poisson's ratio ν :

$$\kappa = \frac{E}{2(1-2\nu)}, \quad \mu = \frac{E}{3(1+\nu)} \quad (5)$$

¹⁵¹ In accordance with the Galerkin formulation, the weak form can be given
¹⁵² by: Find $\mathbf{u} \in V, p \in Q$, such that

$$\begin{cases} a(\mathbf{v}, \mathbf{u}) + b(\mathbf{v}, p) = f(\mathbf{v}) & \forall \mathbf{v} \in V \\ b(\mathbf{u}, q) + c(q, p) = 0 & \forall q \in Q \end{cases} \quad (6)$$

¹⁵³ with the spaces V, Q defined by:

$$V = \{\mathbf{v} \in H^1(\Omega)^2 \mid \mathbf{v} = \mathbf{g}, \text{ on } \Gamma_g\} \quad (7)$$

$$Q = \{q \in L^2(\Omega) \mid \int_{\Omega} q d\Omega = 0\} \quad (8)$$

¹⁵⁴ where $a : V \times V \rightarrow \mathbb{R}$, $b : V \times Q \rightarrow \mathbb{R}$ and $c : Q \times Q \rightarrow \mathbb{R}$ are bilinear forms,
¹⁵⁵ and $f : V \rightarrow \mathbb{R}$ is the linear form. In elasticity problems, they are given by:

$$a(\mathbf{v}, \mathbf{u}) = \int_{\Omega} \nabla^d \mathbf{v} : \nabla^d \mathbf{u} d\Omega \quad (9)$$

$$b(\mathbf{v}, q) = \int_{\Omega} \nabla \cdot \mathbf{v} q d\Omega \quad (10)$$

$$c(q, p) = - \int_{\Omega} \frac{1}{3\kappa} q p d\Omega \quad (11)$$

$$f(\mathbf{v}) = \int_{\Gamma_t} \mathbf{v} \cdot \mathbf{t} d\Gamma + \int_{\Omega} \mathbf{v} \cdot \mathbf{b} d\Omega \quad (12)$$

¹⁵⁶ 2.2. Ritz–Galerkin problem and volumetric locking

¹⁵⁷ In the mixed-formulation framework, the displacement and pressure can be
¹⁵⁸ discretized by different approximations. The approximant displacement \mathbf{u}_h and
¹⁵⁹ approximant pressure p_h can be expressed by:

$$\mathbf{u}_h(\mathbf{x}) = \sum_{I=1}^{n_u} N_I(\mathbf{x}) \mathbf{u}_I, \quad p_h(\mathbf{x}) = \sum_{K=1}^{n_p} \Psi_K(\mathbf{x}) p_K \quad (13)$$

¹⁶⁰ where N_I and Ψ_K are the shape functions for the displacement and pressure, \mathbf{u}_I
¹⁶¹ and p_K are the corresponding coefficients. Leading these approximations into
¹⁶² the weak form of Eq. (6) yields the following Ritz–Galerkin problems: Find
¹⁶³ $\mathbf{u}_h \in V_h$, $p_h \in Q_h$, such that

$$\begin{cases} a(\mathbf{v}_h, \mathbf{u}_h) + b(\mathbf{v}_h, p_h) = f(\mathbf{v}_h) & \forall \mathbf{v}_h \in V_h \\ b(\mathbf{u}_h, q_h) + c(q_h, p_h) = 0 & \forall q_h \in Q_h \end{cases} \quad (14)$$

¹⁶⁴ where the spaces $V_h \subseteq V$, $Q_h \subseteq Q$ are defined by:

$$V_h = \{\mathbf{v}_h \in (\text{span}\{N_I\}_{I=1}^{n_u})^{n_d} | \mathbf{v}_{\underline{h}} = \mathbf{g}, \text{ on } \Gamma_g\} \quad (15)$$

$$Q_h = \{q_h \in \text{span}\{\Psi_K\}_{K=1}^{n_p} | \int_{\Omega} q_h d\Omega = 0\} \quad (16)$$

¹⁶⁵ For nearly incompressible material, the Poisson ratio approaches 0.5, and
¹⁶⁶ the bulk modulus κ will tend to infinity based on Eq. (5). Then, the bilinear
¹⁶⁷ form c in Eq. (11) tends to zero. And the weak form of Eq. (14) becomes an
¹⁶⁸ enforcement of the volumetric strain $\nabla \cdot \mathbf{u}_h$ to be zero using the Lagrangian
¹⁶⁹ multiplier method, where p_h is the Lagrangian multiplier.

¹⁷⁰ Furthermore, from the second line of Eq. (14), we have:

$$b(\mathbf{u}_h, q_h) + c(q_h, p_h) = (q_h, \nabla \cdot \mathbf{u}_h) - (q_h, \frac{1}{3\kappa} p_h) = 0, \quad \forall q_h \in Q_h \quad (17)$$

¹⁷¹ or

$$(q_h, 3\kappa \nabla \cdot \mathbf{u}_h - p_h) = 0, \quad \forall q_h \in Q_h \quad (18)$$

¹⁷² where (\bullet, \bullet) is the inner product operator evaluated by:

$$(q, p) := \int_{\Omega} q p d\Omega \quad (19)$$

¹⁷³ Obviously, in Eq. (18), p_h is the orthogonal projection of $3\kappa \nabla \cdot \mathbf{u}_h$ with respect
¹⁷⁴ to the space Q_h [1], and, for further development, we use the nabla notation
¹⁷⁵ with an upper tilde to denote the projection operator, i.e., $p_h = \tilde{\nabla} \cdot \mathbf{u}_h$. In this
¹⁷⁶ circumstance, the bilinear form b in the first line of Eq. (14) becomes:

$$\begin{aligned} b(\mathbf{v}_h, p_h) &= (\underbrace{\nabla \cdot \mathbf{v}_h - \tilde{\nabla} \cdot \mathbf{v}_h, p_h}_0) + (\tilde{\nabla} \cdot \mathbf{v}_h, \underbrace{p_h}_{3\kappa \tilde{\nabla} \cdot \mathbf{u}_h}) \\ &= (\tilde{\nabla} \cdot \mathbf{v}_h, 3\kappa \tilde{\nabla} \cdot \mathbf{u}_h) \\ &= \tilde{a}(\mathbf{v}_h, \mathbf{u}_h) \end{aligned} \quad (20)$$

¹⁷⁷ where the bilinear form $\tilde{a} : V_h \times V_h \rightarrow \mathbb{R}$ is defined by:

$$\tilde{a}(\mathbf{v}_h, \mathbf{u}_h) = \int_{\Omega} 3\kappa \tilde{\nabla} \cdot \mathbf{v}_h \tilde{\nabla} \cdot \mathbf{u}_h d\Omega \quad (21)$$

¹⁷⁸ Accordingly, the problem of Eq. (14) becomes a one-variable form: Find
¹⁷⁹ $\mathbf{u}_h \in V_h$, such that

$$a(\mathbf{v}_h, \mathbf{u}_h) + \tilde{a}(\mathbf{v}_h, \mathbf{u}_h) = f(\mathbf{v}_h), \quad \forall \mathbf{v}_h \in V_h \quad (22)$$

¹⁸⁰ As $\kappa \rightarrow \infty$, Eq. (22) can be regarded as an enforcement of volumetric strain
¹⁸¹ using the penalty method, where \tilde{a} is the penalty term. However, it should
¹⁸² be noted that, if the mixed-formulation wants to obtain a satisfactory result,
¹⁸³ this orthogonal projection must be surjective [57]. In the case where it is not
¹⁸⁴ surjective, for a given $p_h \in Q_h$, it may not be possible to find a $\mathbf{u}_h \in V_h$ such that
¹⁸⁵ $p_h = 3\kappa \nabla \cdot \mathbf{u}_h$. This will lead to a much smaller displacement than expected and
¹⁸⁶ an oscillated pressure result. This phenomenon is called volumetric locking.

¹⁸⁷ 3. Optimal volumetric constraint ratio

¹⁸⁸ 3.1. Inf-sup condition and its eigenvalue problem

¹⁸⁹ To ensure the surjectivity of orthogonal projection and satisfactory results,
¹⁹⁰ the approximations of Eq.(7) should satisfy the inf-sup condition, also known
¹⁹¹ as the Ladyzhenskaya–Babuška–Brezzi condition [4]:

$$\inf_{q_h \in Q_h} \sup_{\mathbf{v}_h \in V_h} \frac{|b(q_h, \mathbf{v}_h)|}{\|q_h\|_Q \|\mathbf{v}_h\|_V} \geq \beta > 0 \quad (23)$$

¹⁹² in which β , namely the inf-sup value, is a constant independent of the character-
¹⁹³ ized element size h . The Appendix A lists the displacement and pressure error
¹⁹⁴ estimators for mixed-formulations. These estimators imply how the inf-sup

¹⁹⁵ value β affects solution's accuracy. The norms $\|\bullet\|_V$ and $\|\bullet\|_Q$ can be flexibly
¹⁹⁶ defined by:

$$\|\mathbf{v}\|_V^2 := \int_{\Omega} \nabla^d \mathbf{v} : \nabla^d \mathbf{v} d\Omega \quad (24)$$

$$\|q\|_Q^2 := \int_{\Omega} \frac{1}{3\kappa} q^2 d\Omega \quad (25)$$

¹⁹⁷ To establish the relationship between the inf-sup condition and the con-
¹⁹⁸ straint ratio, the inf-sup condition is firstly transformed by the following Lemma
¹⁹⁹ 1:

²⁰⁰ **Lemma 1.** Suppose $\mathcal{P}_h : V_h \rightarrow Q_h$ is the orthogonal projection operator of the
²⁰¹ divergence operator $\mathcal{P} := 3\kappa \nabla \cdot$, i.e., $\mathcal{P}_h := 3\kappa \bar{\nabla} \cdot$ and satisfies Eq. (18). Then,
²⁰² the inf-sup value can be estimated by:

$$\beta \leq \inf_{V'_h \subset V_h \setminus \ker \mathcal{P}_h} \sup_{\mathbf{v}_h \in V'_h} \frac{\|\mathcal{P}_h \mathbf{v}_h\|_Q}{\|\mathbf{v}_h\|_V} \quad (26)$$

²⁰³ in which $\ker \mathcal{P}_h \subset V_h$ is the kernel of \mathcal{P}_h defined by $\ker \mathcal{P}_h := \{\mathbf{v}_h \in V_h \mid \mathcal{P}_h \mathbf{v}_h = 0\}$.

²⁰⁵ PROOF. First, define the image space of \mathcal{P}_h as $\text{Im} \mathcal{P}_h := \{p_h \in Q_h \mid \exists \mathbf{v}_h \in V_h, p_h = \mathcal{P}_h \mathbf{v}_h\}$. Since $\mathcal{P}_h \subset Q_h$, Eq. (23) can be rewritten as:

$$\begin{aligned} \beta &\leq \inf_{q_h \in Q_h} \sup_{\mathbf{v}_h \in V_h} \frac{|b(q_h, \mathbf{v}_h)|}{\|q_h\|_Q \|\mathbf{v}_h\|_V} = \inf_{q_h \in Q_h} \sup_{\mathbf{v}_h \in V_h} \frac{|(q_h, \frac{1}{3\kappa} \mathcal{P} \mathbf{v}_h)|}{\|q_h\|_Q \|\mathbf{v}_h\|_V} \\ &\leq \inf_{q_h \in \text{Im} \mathcal{P}_h} \sup_{\mathbf{v}_h \in V_h} \frac{|\frac{1}{3\kappa} (q_h, \mathcal{P}_h \mathbf{v}_h)|}{\|q_h\|_Q \|\mathbf{v}_h\|_V} \end{aligned} \quad (27)$$

²⁰⁷ For a given $q_h \in \text{Im} \mathcal{P}_h$, since both q_h and $\mathcal{P}_h \mathbf{v}_h$ belong to $\text{Im} \mathcal{P}_h$, $\text{Im} \mathcal{P}_h \subset Q_h$,
²⁰⁸ according to the Cauchy-Schwarz inequality, we have:

$$\left| \frac{1}{3\kappa} (q_h, \mathcal{P}_h \mathbf{v}_h) \right| \leq \|q_h\|_Q \|\mathcal{P}_h \mathbf{v}_h\|_Q \quad (28)$$

²⁰⁹ where this equality holds if and only if $q_h = \mathcal{P}_h \mathbf{v}_h$, i.e.,

$$\left| \frac{1}{3\kappa} (q_h, \mathcal{P}_h \mathbf{v}_h) \right| = \|q_h\|_Q \|\mathcal{P}_h \mathbf{v}_h\|_Q, \quad \forall \mathbf{v}_h \in V'_h \quad (29)$$

²¹⁰ the space $V'_h \subseteq V_h \setminus \ker \mathcal{P}_h$ defined by:

$$V'_h = \{\mathbf{v}_h \in V_h \mid \mathcal{P}_h \mathbf{v}_h = q_h\} \quad (30)$$

²¹¹ And the following relationship can be evidenced:

$$\sup_{\mathbf{v}_h \in V_h} \frac{|\frac{1}{3\kappa} (q_h, \mathcal{P}_h \mathbf{v}_h)|}{\|q_h\|_Q \|\mathbf{v}_h\|_V} = \sup_{\mathbf{v}_h \in V'_h} \frac{\|\mathcal{P}_h \mathbf{v}_h\|_Q}{\|\mathbf{v}_h\|_V}, \quad \exists q_h \in \text{Im} \mathcal{P}_h \quad (31)$$

²¹² Consequently, by combining Eqs. (27) and (31), Eq. (26) can be obtained.

213 **Remark 1.** With Lemma 1 and the norm definitions in Eqs. (24),(25), the
214 square of the inf-sup value can further be bounded by:

$$\beta^2 \leq \inf_{V'_h \subset V_h \setminus \ker \mathcal{P}_h} \sup_{\mathbf{v}_h \in V'_h} \frac{\|\mathcal{P}_h \mathbf{v}_h\|_Q^2}{\|\mathbf{v}_h\|_V^2} = \inf_{V'_h \subset V_h \setminus \ker \mathcal{P}_h} \sup_{\mathbf{v}_h \in V'_h} \frac{\tilde{a}(\mathbf{v}_h, \mathbf{v}_h)}{a(\mathbf{v}_h, \mathbf{v}_h)} \quad (32)$$

215 The left-hand side of the above equation is consistent with the minimum-maximum
216 principle [58] and again proves the equivalence with the traditional numerical
217 inf-sup test [5]. Since that, β^2 evaluates the non-zero general eigenvalue of \tilde{a}
218 and a in Eq. (22).

219 3.2. Inf-sup value estimator

220 Subsequently, the relationship between constraint ratio and the inf-sup con-
221 dition is established by the following Theorem:

222 **Theorem 1.** Suppose that P_{n_u} is a complete polynomial space with n_u dimen-
223 sions, and V_{n_u} is the polynomial displacement space, $V_{n_u} = P_{n_u}^{n_d}$. The inf-sup
224 value β can further be bounded by:

$$\beta \leq \beta_s + O(h) \quad (33)$$

225 with

$$\beta_s = \inf_{V' \subset V_{n_u} \setminus \ker \mathcal{P}_h \mathcal{I}_h} \sup_{\mathbf{v} \in V'} \frac{\|\mathcal{P} \mathbf{v}\|_Q}{\|\mathbf{v}\|_V} \quad (34)$$

226 where \mathcal{I}_h is the interpolation operator of the displacement approximation, and
227 correspondingly, $O(h)$ is the remainder related to h .

228 PROOF. As the dimensions of V_h and V_{n_u} are identical, $\dim V_{n_u} = \dim V_h =$
229 $n_d \times n_u$. There exists a unique $\mathbf{v} \in V_{n_u}$ satisfying $\mathbf{v}_h = \mathcal{I}_h \mathbf{v}$. And the right side
230 of Eq. (26) becomes:

$$\inf_{V'_h \subset V_h \setminus \ker \mathcal{P}_h} \sup_{\mathbf{v}_h \in V'_h} \frac{\|\mathcal{P}_h \mathbf{v}_h\|_Q}{\|\mathbf{v}_h\|_V} = \inf_{V' \subset V_{n_u} \setminus \ker \mathcal{P}_h \mathcal{I}_h} \sup_{\mathbf{v} \in V'} \frac{\|\mathcal{P}_h \mathcal{I}_h \mathbf{v}\|_Q}{\|\mathcal{I}_h \mathbf{v}\|_V} \quad (35)$$

231 According to the triangular inequality, Cauchy-Schwarz inequality, and the
232 relationship of Eqs. (18), we have:

$$\begin{aligned} \|\mathcal{P}_h \mathcal{I}_h \mathbf{v}\|_Q &= \sup_{q_h \in Q_h} \frac{|\frac{1}{3\kappa}(q_h, \mathcal{P}_h \mathcal{I}_h \mathbf{v})|}{\|q_h\|_Q} = \sup_{q_h \in Q_h} \frac{|\frac{1}{3\kappa}(q_h, \mathcal{P} \mathcal{I}_h \mathbf{v})|}{\|q_h\|_Q} \\ &\leq \sup_{q_h \in Q_h} \frac{|\frac{1}{3\kappa}(q_h, \mathcal{P} \mathbf{v})| + |\frac{1}{3\kappa}(q_h, \mathcal{P} \mathbf{v} - \mathcal{P} \mathcal{I}_h \mathbf{v})|}{\|q_h\|_Q} \\ &\leq \|\mathcal{P} \mathbf{v}\|_Q + \|\mathcal{P}(\mathbf{v} - \mathcal{I}_h \mathbf{v})\|_Q \end{aligned} \quad (36)$$

233 Obviously, the second term on the right side of Eq. (36) is the interpolation
234 error, and can be evaluated by [59]:

$$\|\mathcal{P}(\mathbf{v} - \mathcal{I}_h \mathbf{v})\|_Q \leq Ch^k |\mathbf{v}|_{H_k} \quad (37)$$

235 where, for a sufficiently smooth $\mathbf{v} \in V$, k equals to the interpolation order of
 236 \mathcal{I}_h .

237 Further leading the relation $\|\mathcal{I}_h \mathbf{v}\|_V \geq C|\mathbf{v}|_{H_k}$ obtained from the closed
 238 graph theorem [33] and considering Eqs. (36)-(37), the right-hand side of Eq.
 239 (35) can be represented as:

$$\inf_{V' \subset V_{n_u} \setminus \ker \mathcal{P}_h \mathcal{I}_h} \sup_{\mathbf{v} \in V'} \frac{\|\mathcal{P}_h \mathcal{I}_h \mathbf{v}\|_Q}{\|\mathcal{I}_h \mathbf{v}\|_V} \leq \inf_{V' \subset V_{n_u} \setminus \ker \mathcal{P}_h \mathcal{I}_h} \sup_{\mathbf{v} \in V'} \frac{\|\mathcal{P} \mathbf{v}\|_Q}{\|\mathbf{v}\|_V} + O(h) \quad (38)$$

240 Substituting Eqs. (35),(38) into (26) finally proves Eqs. (33), (34).

241 As we can see in Eqs. (33) and (34), $\beta_s \geq 0$, the condition that β_s being
 242 equal to 0 or not determines whether the formulation can satisfy the inf-sup
 243 condition. If $\beta_s > 0$, as the mesh refines, the second term on the right-hand
 244 side of Eq. (33) will sharply reduce and can be ignored. In contrast, if $\beta_s = 0$,
 245 the second term will dominate, and the evaluation of β will be dependent to h .
 246 Therefore, the inf-sup condition is violated and numerical instability arises.

247 3.3. Polynomial-wise constraint counting

248 From the above subsection, we can know that whether β_s is zero or not
 249 determines whether the mixed-formulation can fulfill the inf-sup condition. Ac-
 250 cording to the expression of β_s in Eq. (34), as $\beta_s = 0$, the variable \mathbf{v} should
 251 belong to $\ker \mathcal{P}$, so the dimensions of the subspace in which $\beta_s \neq 0$, namely n_s ,
 252 can be evaluated by:

$$n_s = \dim(V_{n_u} \setminus \ker \mathcal{P}) \quad (39)$$

253 To further construct the relationship between the inf-sup value estimator in
 254 Eq. (33) and the constraint ratio $r = \frac{n_d \times n_u}{n_p}$, we should find the displacement
 255 and pressure DOFs in Eq. (33). With the definition of V_{n_u} , the number of
 256 displacement DOFs is easy to be evaluated by:

$$n_d \times n_u = \dim V_{n_u} \quad (40)$$

257 With well-posed nodal distributions of displacement and pressure, the number
 258 of pressure DOFs has the following relationship:

$$n_p = \dim Q_h = \dim(\text{Im} \mathcal{P}_h) = \dim(V_{n_u} \setminus \ker \mathcal{P}_h \mathcal{I}_h) \quad (41)$$

259 Figure 1 illustrates how the relationship between n_s , n_p , and n_u influences
 260 the fulfillment of the inf-sup condition:

- 261 • As $n_p > n_s$, there must exist a subspace in space $V_{n_u} \setminus \ker \mathcal{P}_h \mathcal{I}_h$ belonging
 262 to $\ker \mathcal{P}$, resulting in $\beta_s = 0$, i.e., $V_{n_u} \setminus \ker \mathcal{P}_h \mathcal{I}_h \cap \ker \mathcal{P} \neq \emptyset$. At this cir-
 263 cumstance, the inf-sup condition cannot be satisfied, and the formulation
 264 will suffer from volumetric locking.
- 265 • As $n_p \leq n_s$, for well-posed nodal distributions, the space $V_{n_u} \setminus \ker \mathcal{P}_h \mathcal{I}_h$
 266 may be a subset of $V_{n_u} \setminus \ker \mathcal{P}$. Then, β_s will remain nonzero, and the
 267 formulation will be locking-free.

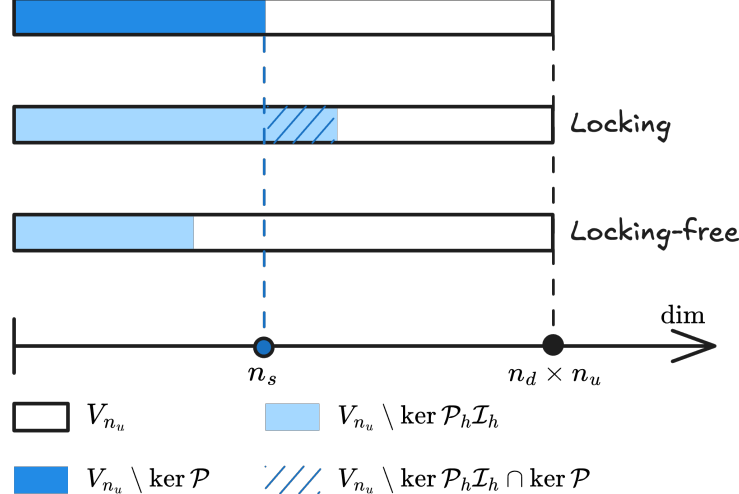


Figure 1: Illustration of estimator

268 Summarily, the formulation can satisfy the inf-sup condition and alleviate
 269 volumetric locking if at least the number of pressure nodes n_p is less than n_s ,
 270 so we name n_s as the stabilized number of pressure nodes. At this moment,
 271 the volumetric constraint ratio should meet the following relation to ensure the
 272 inf-sup condition:

$$r_{opt} \geq \frac{n_d \times n_u}{n_s} \quad (42)$$

273 **Remark 2.** *Some uniform elements with special arrangements, like the union-*
 274 *jack element arrangement for 3-node triangular elements, can pass the inf-sup*
 275 *test [6], but their pressure DOFs number is greater than n_s . This is because the*
 276 *union-jack arrangement leads to a lower nonzero eigenvalue number of $\tilde{\alpha}$ and a*
 277 *in Eq. (22), and the corresponding nonzero eigenvalue number is less than or*
 278 *equal to the stabilized number n_s , satisfying Eq. (42). The similar cases about*
 279 *this special element arrangement are too few, so it is more straightforward to*
 280 *use the number of pressure nodes n_p to measure $\dim(V_{n_u} \setminus \ker \mathcal{P}_h \mathcal{I}_h)$.*

281 **Remark 3.** *It is obvious that the traditional optimal constraint ratio cannot*
 282 *fulfill this condition. However, not all formulations satisfying this condition can*
 283 *totally avoid volumetric locking. This is because $n_p \leq n_s$ is not equivalent to*
 284 *$V_{n_u} \setminus \ker \mathcal{P}_h \mathcal{I}_h \subset V_{n_u} \setminus \ker \mathcal{P}$. Fortunately, well-posed nodal distributions of*
 285 *displacement and pressure can ensure this, which will be evidenced by numerical*
 286 *examples in the subsequent sections.*

287 3.4. Optimal volumetric constraint ratio

288 The fulfillment of the inf-sup condition should require the number of pres-
 289 sure nodes n_p to be lower than the stabilized number n_s , and now, we will
 290 demonstrate how to determine n_s for a specific number of displacement DOFs.

²⁹¹ In the 2D case, for instance, we first consider the linear polynomial displace-
²⁹² ment space V_3 that is given by:

$$V_3 = \text{span} \left\{ \begin{pmatrix} 1 \\ 0 \end{pmatrix}, \begin{pmatrix} 0 \\ 1 \end{pmatrix}, \begin{pmatrix} x \\ 0 \end{pmatrix}, \begin{pmatrix} 0 \\ x \end{pmatrix}, \begin{pmatrix} y \\ 0 \end{pmatrix}, \begin{pmatrix} 0 \\ y \end{pmatrix} \right\} \quad (43)$$

²⁹³ or rearranged as follows,

$$V_3 = \text{span} \left\{ \underbrace{\begin{pmatrix} 1 \\ 0 \end{pmatrix}, \begin{pmatrix} 0 \\ 1 \end{pmatrix}, \begin{pmatrix} y \\ 0 \end{pmatrix}, \begin{pmatrix} 0 \\ x \end{pmatrix}, \begin{pmatrix} x \\ -y \end{pmatrix}}_{\ker \mathcal{P}}, \underbrace{\begin{pmatrix} x \\ y \end{pmatrix}}_{V_3 \setminus \ker \mathcal{P}} \right\} \quad (44)$$

²⁹⁴ It can be counted that, for $n_u = 3$, $n_s = 1$. Following the path, the displacement
²⁹⁵ space with a quadratic polynomial base, namely V_6 , can be stated as:

$$V_6 = \text{span} \left\{ \underbrace{\begin{pmatrix} 1 \\ 0 \end{pmatrix}, \begin{pmatrix} 0 \\ 1 \end{pmatrix}, \begin{pmatrix} y \\ 0 \end{pmatrix}, \begin{pmatrix} 0 \\ x \end{pmatrix}, \begin{pmatrix} x \\ -y \end{pmatrix}, \begin{pmatrix} x^2 \\ -2xy \end{pmatrix}, \begin{pmatrix} y^2 \\ 0 \end{pmatrix}, \begin{pmatrix} 0 \\ x^2 \end{pmatrix}, \begin{pmatrix} -2xy \\ y^2 \end{pmatrix}}_{\ker \mathcal{P}}, \underbrace{\begin{pmatrix} x \\ y \end{pmatrix}, \begin{pmatrix} x^2 \\ 2xy \end{pmatrix}, \begin{pmatrix} 2xy \\ y^2 \end{pmatrix}}_{V_6 \setminus \ker \mathcal{P}} \right\} \quad (45)$$

²⁹⁶ In this circumstance, $n_s = 3$. As the order of the polynomial space increases,
²⁹⁷ the optimal numbers of constraint DOFs for each order of the polynomial space
²⁹⁸ are listed in Table. 1, in which n denotes the order of space P_{n_u} . For the
²⁹⁹ flexibility of usage, the relation between n_u and n_s is summarized as follows:

$$n_s = \frac{n(n+1)}{2}, \quad n = \left\lfloor \frac{\sqrt{1+8n_u}-3}{2} \right\rfloor \quad (46)$$

³⁰⁰ where $\lfloor \bullet \rfloor$ denotes the floor function.

Table 1: Relationship between the number of displacement nodes n_u and stabilized number of pressure nodes n_s

n	2D		3D	
	n_u	n_s	n_u	n_s
1	3	1	4	1
2	6	3	10	4
3	10	6	20	10
4	15	10	35	20
\vdots	\vdots	\vdots	\vdots	\vdots

³⁰¹ For the 3D case, following the path in 2D, the linear polynomial space V_4 is

302 considered herein, and the arranged space of V_4 is listed as follows:

$$V_4 = \text{span} \left\{ \underbrace{\begin{pmatrix} 1 \\ 0 \\ 0 \\ 0 \end{pmatrix}, \begin{pmatrix} 0 \\ 1 \\ 0 \\ 0 \end{pmatrix}, \begin{pmatrix} 0 \\ 0 \\ 1 \\ 0 \end{pmatrix}, \begin{pmatrix} 0 \\ x \\ 0 \\ 0 \end{pmatrix}, \begin{pmatrix} 0 \\ 0 \\ x \\ 0 \end{pmatrix}, \begin{pmatrix} y \\ 0 \\ 0 \\ 0 \end{pmatrix}}_{\ker \mathcal{P}}, \underbrace{\begin{pmatrix} 0 \\ 0 \\ z \\ 0 \end{pmatrix}, \begin{pmatrix} 0 \\ 0 \\ z \\ 0 \end{pmatrix}, \begin{pmatrix} 0 \\ 0 \\ 0 \\ z \end{pmatrix}, \begin{pmatrix} x \\ -y \\ 0 \\ 0 \end{pmatrix}, \begin{pmatrix} x \\ 0 \\ -z \\ 0 \end{pmatrix}, \begin{pmatrix} x \\ y \\ z \\ 0 \end{pmatrix}}_{\ker \mathcal{P}}, \underbrace{\begin{pmatrix} 0 \\ 0 \\ 0 \\ 0 \end{pmatrix}}_{V_{n_u} \setminus \ker \mathcal{P}} \right\} \quad (47)$$

303 For brevity, the stabilized numbers for higher-order polynomial displacement
 304 spaces are directly listed in Table. 1, and it can be summarized that, for a given
 305 number of displacement DOFs, the stabilized number for pressure DOFs can be
 306 calculated as follows:

$$n_s = \frac{n(n+1)(n+2)}{6} \quad (48)$$

$$n = \left[\left(3n_u + \frac{1}{3} \sqrt{81n_u^2 - \frac{1}{3}} \right)^{\frac{1}{3}} + \frac{1}{3 \left(3n_u + \frac{1}{3} \sqrt{81n_u^2 - \frac{1}{3}} \right)^{\frac{1}{3}}} - 2 \right] \quad (49)$$

307 [Table 2 lists the effectiveness of the traditional constraint ratio and the](#)
 308 [proposed optimal constraint ratio for traditional mixed formulation schemes,](#)
 309 [comparing the constraint ratios with the fulfillment of the inf-sup condition](#)
 310 [using analytical proof and numerical prediction. The table reveals that the](#)
 311 [traditional constraint ratio \$r \geq n_d\$ is not sufficient to guarantee the inf-sup](#)
 312 [condition, especially for Q4P1 and Q8P3. The proposed optimal constraint](#)
 313 [ratio \$r_{opt} > \frac{n_d \times n_u}{n_s}\$ is more effective in ensuring the inf-sup condition, since the](#)
 314 [corresponding results is consistent with numerical prediction or analytical proof](#)
 315 [of inf-sup condition.](#)

316 4. Mixed FE–meshfree formulation with optimal constraint ratio

317 In the proposed mixed–formulation, the displacement is approximated using
 318 3-node (Tri3), 6-node (Tri6) triangular elements and 4-node (Quad4), 8-node
 319 (Quad8) quadrilateral elements in 2D, 4-node (Tet4) tetrahedral element and
 320 8-node (Hex8) hexahedral element in 3D [2]. In order to flexibly adjust to let
 321 the DOFs of pressure meet the optimal constraint, the reproducing kernel (RK)
 322 meshfree approximation is involved to approximate pressure, [namely FE–RK](#)
 323 [formulation.](#)

324 4.1. Reproducing kernel meshfree approximation

325 In accordance with the reproducing kernel approximation, the entire domain
 326 Ω , as shown in Figure 2, is discretized by n_p meshfree nodes, $\{\mathbf{x}_I\}_{I=1}^{n_p}$. The

Table 2: Inf-sup condition and constraint ratio for various mixed formulations

Formulation	Inf-sup condition		Constraint Ratio	
	Numerical prediction	Analytical proof	$r \geq n_d$	$r = r_{opt}$
TSP1($r = 1$)	✗	✗	✗	✗
Q4P1($r = 2$)	✗	✗	✓	✗
Q8P3($r = 2$)	✗	✗	✓	✗
Q8P1($r = 6$)	✓	✓	✓	✓
Q9P3($r = \frac{8}{3}$)	✓	✓	✓	✓
MINI($r = 6$)	✓	✓	✓	✓
Taylor-Hood($r = 8$)	✓	✓	✓	✓
T6C3($r = 8$)	✓	✓		✓


: Displacement node
: Pressure node

³²⁷ approximated pressure, namely p_h , can be expressed by the shape function Ψ_I
³²⁸ and nodal coefficient p_I , yields:

$$p_h(\mathbf{x}) = \sum_{I=1}^{n_p} \Psi_I(\mathbf{x}) p_I \quad (50)$$

³²⁹ where, in the reproducing kernel approximation framework, the shape function
³³⁰ Ψ_I is given by:

$$\Psi_I(\mathbf{x}) = \mathbf{c}(\mathbf{x}_I - \mathbf{x}) \mathbf{p}(\mathbf{x}_I - \mathbf{x}) \phi(\mathbf{x}_I - \mathbf{x}) \quad (51)$$

³³¹ in which \mathbf{p} is the basis vector, for instance in the context of the 3D quadratic
³³² case, the basis vector takes the following form:

$$\mathbf{p}(\mathbf{x}) = \{1, x, y, z, x^2, y^2, z^2, xy, xz, yz\}^T \quad (52)$$

³³³ and ϕ stands for the kernel function. In this work, the traditional Cubic B-spline
³³⁴ function with square or cube support is used as the kernel function:

$$\phi(\mathbf{x}_I - \mathbf{x}) = \phi(s_x) \phi(s_y) \phi(s_z), \quad s_i = \frac{\|\mathbf{x}_I - \mathbf{x}\|}{\bar{s}_{iI}} \quad (53)$$

³³⁵ with

$$\phi(s) = \frac{1}{3!} \begin{cases} (2-2s)^3 - 4(1-2s)^3 & s \leq \frac{1}{2} \\ (2-2s)^3 & \frac{1}{2} < s < 1 \\ 0 & s > 1 \end{cases} \quad (54)$$

³³⁶ where \bar{s}_{iI} 's are the support size towards the i -direction for the shape function
³³⁷ Ψ_I . The correction function \mathbf{c} can be determined by the following so-called
³³⁸ consistency condition:

$$\sum_{I=1}^{n_p} \Psi_I(\mathbf{x}) \mathbf{p}(\mathbf{x}_I) = \mathbf{p}(\mathbf{x}) \quad (55)$$

³³⁹ or equivalent shifted form:

$$\sum_{I=1}^{n_p} \Psi_I(\mathbf{x}) \mathbf{p}(\mathbf{x}_I - \mathbf{x}) = \mathbf{p}(\mathbf{0}) \quad (56)$$

³⁴⁰ The consistency condition ensures that the reproducing kernel shape functions
³⁴¹ are able to reproduce the polynomial space spanned by the basis function \mathbf{p} ,
³⁴² which is a fundamental requirement for the accuracy of the Galerkin method.
³⁴³ Herein, the order of the basis function \mathbf{p} is chosen to be the same as the order
³⁴⁴ of the displacement approximation.

³⁴⁵ Further, substituting Eq. 51 into Eq. (56) leads to:

$$\mathbf{c}(\mathbf{x}_I - \mathbf{x}) = \mathbf{A}^{-1}(\mathbf{x}_I - \mathbf{x}) \mathbf{p}(\mathbf{0}) \quad (57)$$

³⁴⁶ in which \mathbf{A} is namely the moment matrix evaluated by:

$$\mathbf{A}(\mathbf{x}_I - \mathbf{x}) = \sum_{I=1}^{n_p} \mathbf{p}(\mathbf{x}_I - \mathbf{x}) \mathbf{p}^T(\mathbf{x}_I - \mathbf{x}) \phi(\mathbf{x}_I - \mathbf{x}) \quad (58)$$

³⁴⁷ Taking Eq. (57) back to Eq. (51), the final form of the reproducing kernel shape
³⁴⁸ function can be obtained as:

$$\Psi_I(\mathbf{x}) = \mathbf{p}^T(\mathbf{0}) \mathbf{A}^{-1}(\mathbf{x}_I - \mathbf{x}) \phi(\mathbf{x}_I - \mathbf{x}) \quad (59)$$

³⁴⁹ As shown in Figure 2, reproducing kernel meshfree shape functions are glob-
³⁵⁰ ally smooth across the entire domain, using them to discretize the pressure field
³⁵¹ allows the constraint ratio to be adjusted arbitrarily, without being limited by
³⁵² element topology. Meshfree shape functions generally lack the Kronecker delta
³⁵³ property, which prevents the direct imposition of essential boundary conditions.
³⁵⁴ Fortunately, the mixed formulation shown in Eq. 14 only concerns the displace-
³⁵⁵ ment essential boundary condition, and this condition can be easily imposed by
³⁵⁶ the standard methods, such as the penalty method that used in this work.

³⁵⁷ Moreover, when combined with finite element approximations in Eq. 14,
³⁵⁸ numerical integration can be conveniently performed within each finite element
³⁵⁹ (Ω_C 's). The numerical integration issue caused by the loss of variational consis-
³⁶⁰ tency between meshfree shape functions and their derivatives [60] would not ap-
³⁶¹ pear in the mixed formulation of Eq. 14, this is due to the fact that Eq. 14 solely
³⁶² depends on the meshfree shape functions themselves. Therefore, the proposed
³⁶³ method employs standard lower-order Gaussian quadrature rules, as commonly
³⁶⁴ used in traditional finite element methods, while still maintaining its accuracy.
³⁶⁵ Table 3 lists the integration schemes used in this work for mixed-formulations.
³⁶⁶ Methods with linear basis functions use an integration scheme of order 2. Those
³⁶⁷ with quadratic basis functions use a scheme of order 4. The detailed locations
³⁶⁸ and weights of the Gauss points can be found in Ref. [4]. A sensitivity study on
³⁶⁹ the integration order is carried out in a further numerical example in Section
³⁷⁰ 5.2. The results from this study demonstrate the efficacy of these integration
³⁷¹ schemes.

Table 3: Integration schemes for the mixed FE–meshfree formulation

Methods	n_o	n_g for Ω	n_g for Γ
Tri3-RK	2	3	2
Tri6-RK	4	6	3
Quad4-RK	2	2×2	2
Quad8-RK	4	3×3	3
Tet4-RK	2	4	3
Hex8-RK	2	$2 \times 2 \times 2$	4

n_o : Integration Order n_g : Number of integration points

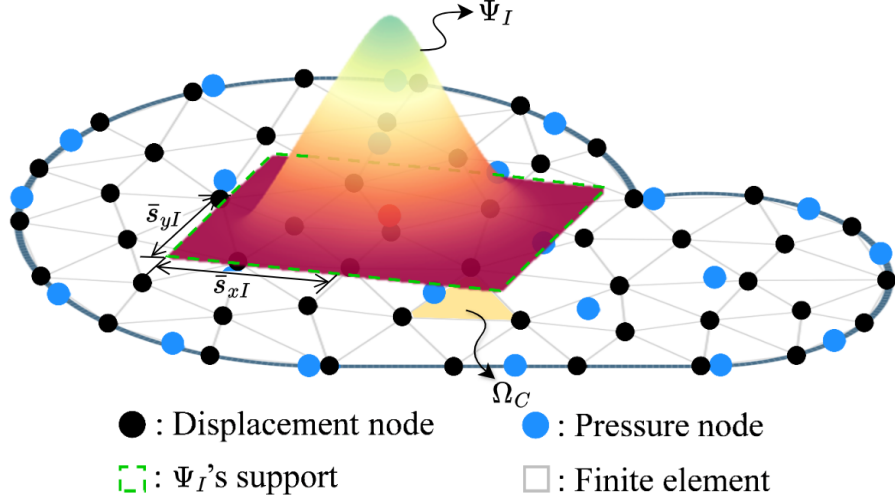


Figure 2: Illustration for reproducing kernel meshfree approximation

³⁷² *4.2. Pressure node distributions with optimal constraint ratio*

³⁷³ In this subsection, 2D and 3D inf-sup tests [6], as defined in Eq. 32, are
³⁷⁴ conducted using the mixed FE-meshfree formulations to validate the proposed
³⁷⁵ inf-sup value estimator. The 2D test considers the square domain $\Omega = (0, 1) \times$
³⁷⁶ $(0, 1)$, where the displacement is discretized by Tri3 and Quad4 with 4×4 ,
³⁷⁷ 8×8 , 16×16 and 32×32 elements, Tri6 and Quad8 with 2×2 , 4×4 , 8×8
³⁷⁸ and 16×16 elements, respectively. The 3D test employs a cube domain $\Omega =$
³⁷⁹ $(0, 1) \times (0, 1) \times (0, 1)$ with 4×4 , 8×8 and 16×16 elements for the Tet4 and Hex8.
³⁸⁰ For pressure discretization, linear meshfree approximation with a normalized
³⁸¹ support size of 1.5 is employed for Tri3, Quad4, Tet4 and Hex8. For Tri6 and
³⁸² Quad8, a quadratic meshfree approximation with a normalized support size of
³⁸³ 2.5 is utilized. In order to avoid the influence of interpolation error, uniform
³⁸⁴ nodal distributions are used for pressure discretizations, for example in Figure
³⁸⁵ 3, which displays 4×4 Quad4 elements with 4×3 uniformly distributed pressure
³⁸⁶ nodes.

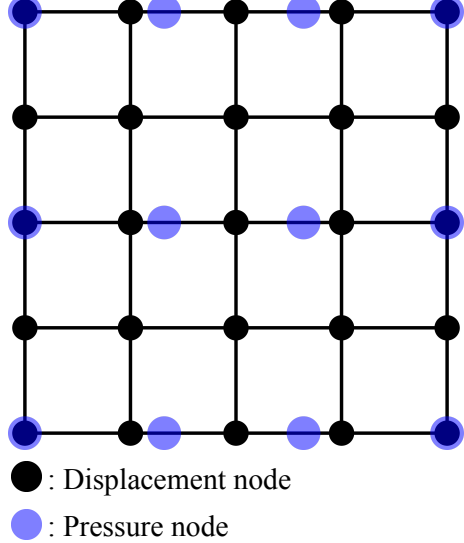


Figure 3: Illustration of uniform nodal distribution for inf-sup test with $n_u = 5 \times 5$, $n_p = 4 \times 3$

Figures 4–9 show the corresponding results, in which the red line stands for the value of β with respect to the number of pressure nodes n_p , and the vertical dashed line denotes the stabilized number n_s . The deeper color of the lines means mesh refinement. The results show that, no matter linear or quadratic elements, as n_p increases over n_s , the value of β sharply decreases, and then the inf-sup condition cannot be maintained. This result is consistent with the discussion in Section 3, and again verifies the effect of the proposed estimator.

Moreover, the mixed formulation's results with the traditional optimal constraint ratio $r = n_d$ are listed in these figures as well, and β in this circumstance is already much smaller than those in the optimal range. Considering the results shown above, the easy programming and efficiency, the pressure nodes are chosen among the displacement nodes. The optimal schemes for linear and quadratic, 2D and 3D element discretizations, namely with $r = r_{opt}$, are shown in Figure 10, where every other displacement node is selected as the pressure node. For practical implementations of linear cases, the pressure nodes are initially generated using traditional approaches, such as Delaunay triangulation. Subsequently, the displacement nodes are then obtained through a standard mesh refinement process to the pressure nodes. For quadratic approximations in Tri6 and Quad8 elements, the element vertices are chosen as pressure nodes after displacement element generation. Consequently, all constraint ratios evaluated using the discretizations in Figure 10 fall within the optimal range. The corresponding inf-sup test results for these schemes are also marked in inf-sup test figure and show that, with mesh refinement, their β 's are always maintained at a non-negligible level.

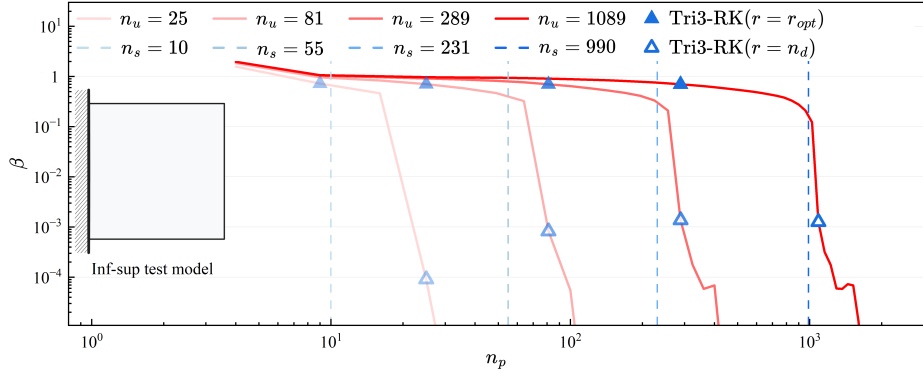


Figure 4: Inf-sup test for Tri3-RK

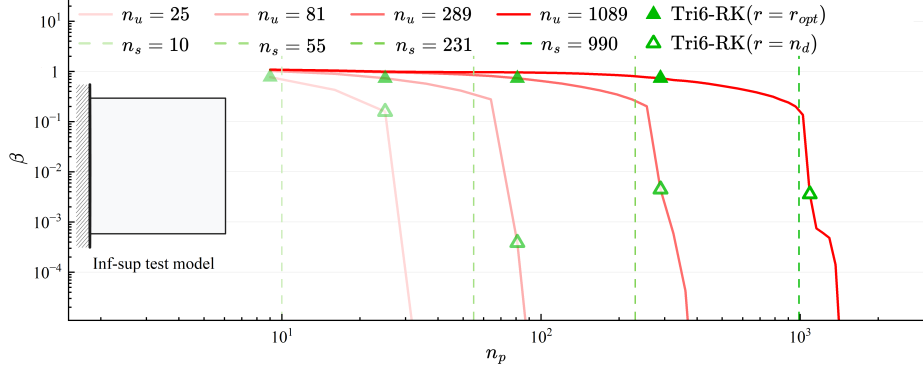


Figure 5: Inf-sup test for Tri6-RK

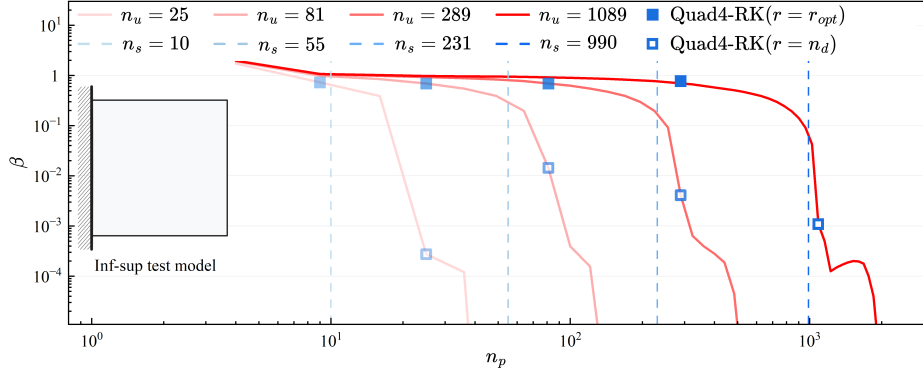


Figure 6: Inf-sup test for Quad4-RK

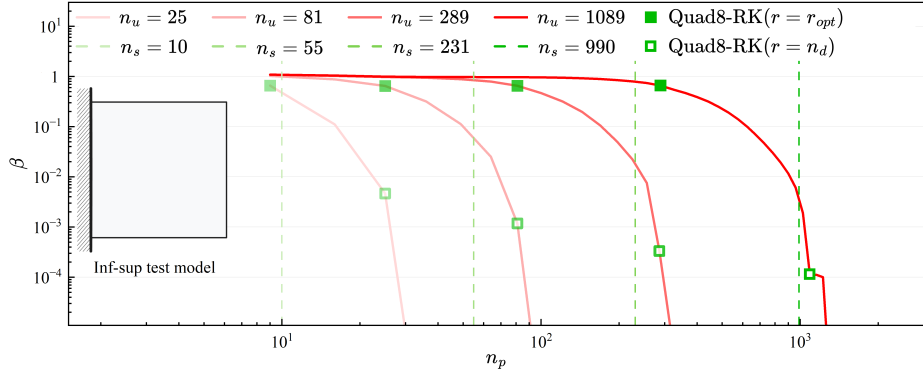


Figure 7: Inf-sup test for Quad8-RK

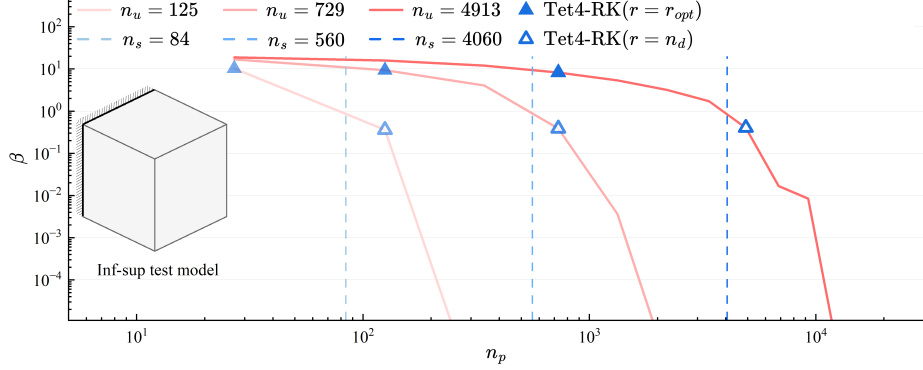


Figure 8: Inf-sup test for Tet4-RK

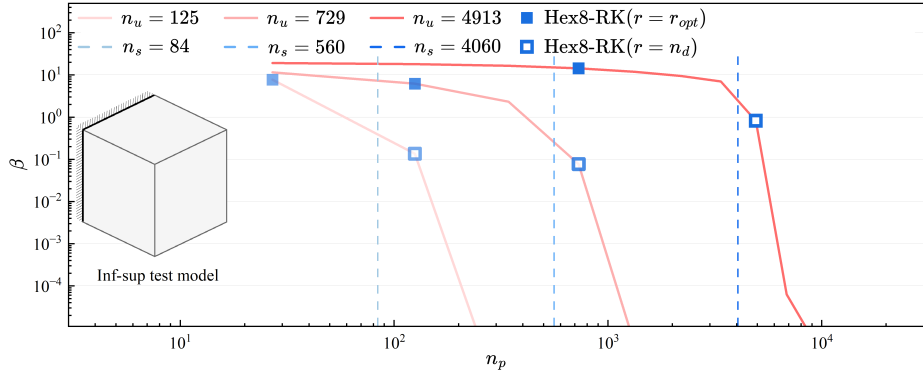


Figure 9: Inf-sup test for Hex8-RK

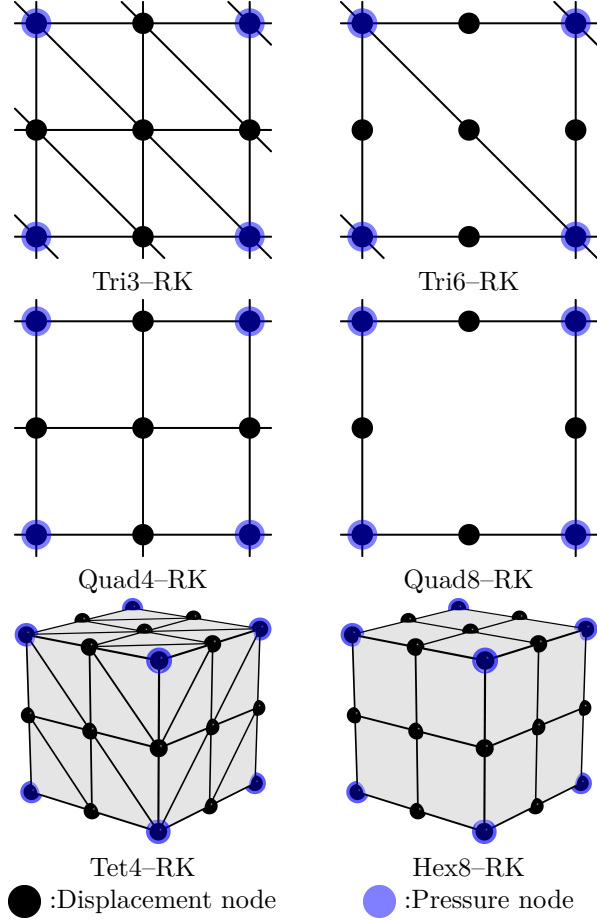


Figure 10: Nodal distribution schemes for mixed FE-meshfree formulations with $r = r_{opt}$

411 5. Numerical examples

412 5.1. Cantilever beam problem

413 Consider the cantilever beam problem shown in Figure 11 with length $L =$
 414 $D = 12$, and the incompressible material parameters are employed
 415 with Young's modulus $E = 3 \times 10^6$, Poisson's ratio $\nu = 0.5 - 10^{-8}$. The left hand
 416 side is fixed and the right side subject to a concentrated force $P = 1000$. All
 417 the prescribed values in the boundary conditions are evaluated by the analytical
 418 solution that is given as follows [61]:

$$\begin{cases} u_x(\mathbf{x}) = -\frac{Py}{6EI} \left((6L - 3x)x + (2 + \bar{\nu})(y^2 - \frac{D^2}{4}) \right) \\ u_y(\mathbf{x}) = \frac{P}{6EI} \left(3\bar{\nu}y^2(L - x) + (4 + 5\bar{\nu})\frac{D^2x}{4} + (3L - x)x^2 \right) \end{cases} \quad (60)$$

419 where I is the beam's moment of inertia, \bar{E} and $\bar{\nu}$ are the material parameters
 420 for plane strain hypothesis, they can be expressed by:

$$I = \frac{D^3}{12}, \quad \bar{E} = \frac{E}{1 - \nu^2}, \quad \bar{\nu} = \frac{\nu}{1 - \nu} \quad (61)$$

421 And correspondingly, the stress components [and the pressure](#) are evaluated by

$$\begin{cases} \sigma_{xx} = -\frac{P(L-x)y}{I} \\ \sigma_{yy} = 0 \\ \sigma_{xy} = \frac{P}{2I} \left(\frac{D^2}{4} - y^2 \right) \\ p = -\frac{P(1+\nu)(L-x)y}{3I} \end{cases} \quad (62)$$

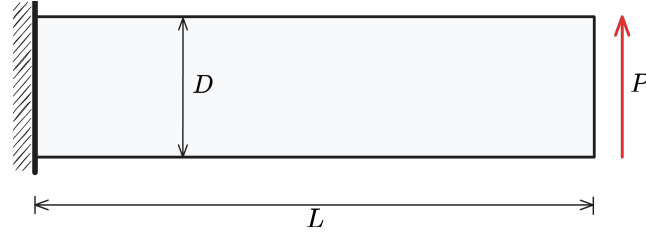


Figure 11: Illustration of cantilever beam problem

422 In this problem, the [Tri3](#), [Quad4](#) [elements](#) with 16×4 , 32×8 , 64×16 , 128×32
 423 grids, and [Tri6](#), [Quad8](#) [elements](#) with 8×2 , 16×4 , 32×8 , 64×16 grids are
 424 employed for displacement discretization. The pressure is discretized by linear
 425 and quadratic meshfree approximations with 1.5 and 2.5 characterized support
 426 sizes respectively. The strain and pressure errors with respect to pressure nodes
 427 n_p are displayed in [Figures 12](#), 13, where, to avoid the interpolation error, the
 428 pressure nodes are uniformly distributed independent with displacement nodes
 429 by the same way in Section 4.2. The vertical dashed lines stand for the stabilized
 430 number n_s . The [figures imply that all pressure errors immediately increase when](#)
 431 [their constraint ratios are out of the optimal range, and quadratic elements still](#)
 432 [have better results than linear elements. It is interesting that the pressure](#)
 433 [errors do not increase as \$n_p\$ becomes very small. This is because the exact](#)
 434 [pressure solution for this problem, given in Eq. \(62\), is only a second-order](#)
 435 [polynomial. Consequently, the pressure interpolation error in Eq. \(A.14\) is](#)
 436 [either very small or nonexistent. In this circumstance, the pressure interpolation](#)
 437 [error is primarily controlled by strain error and inf-sup value \$\beta\$. For the strain](#)
 438 [error, the Quad8-RK method shows stable results regardless of whether the](#)
 439 [constraint ratio is in the optimal range. This may be due to the fact that the](#)
 440 [Quad8 element with a regular mesh satisfies the relationship of Eq. \(A.16\). In](#)

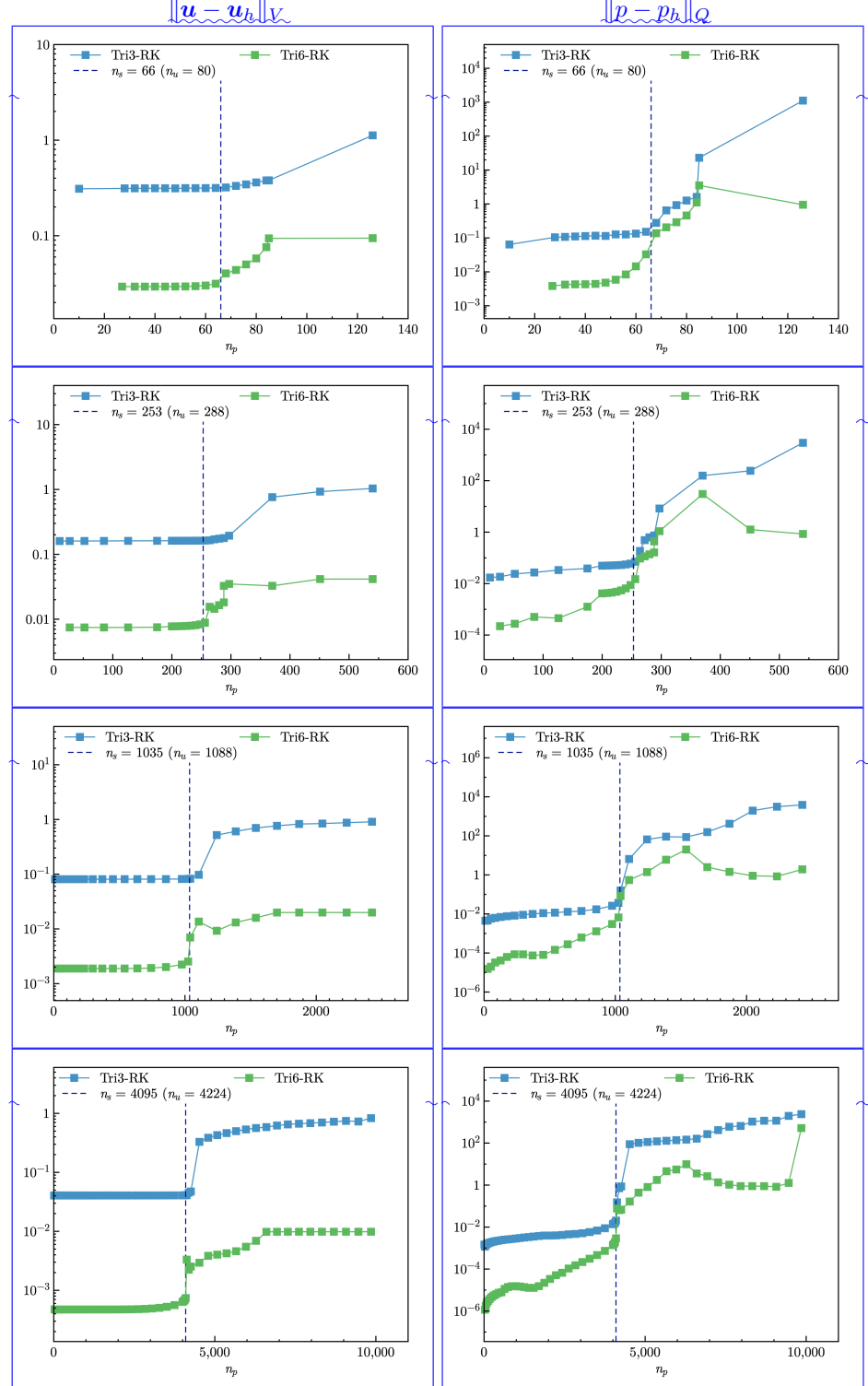


Figure 12: Strain and pressure errors vs. n_p for cantilever beam problem with triangular elements

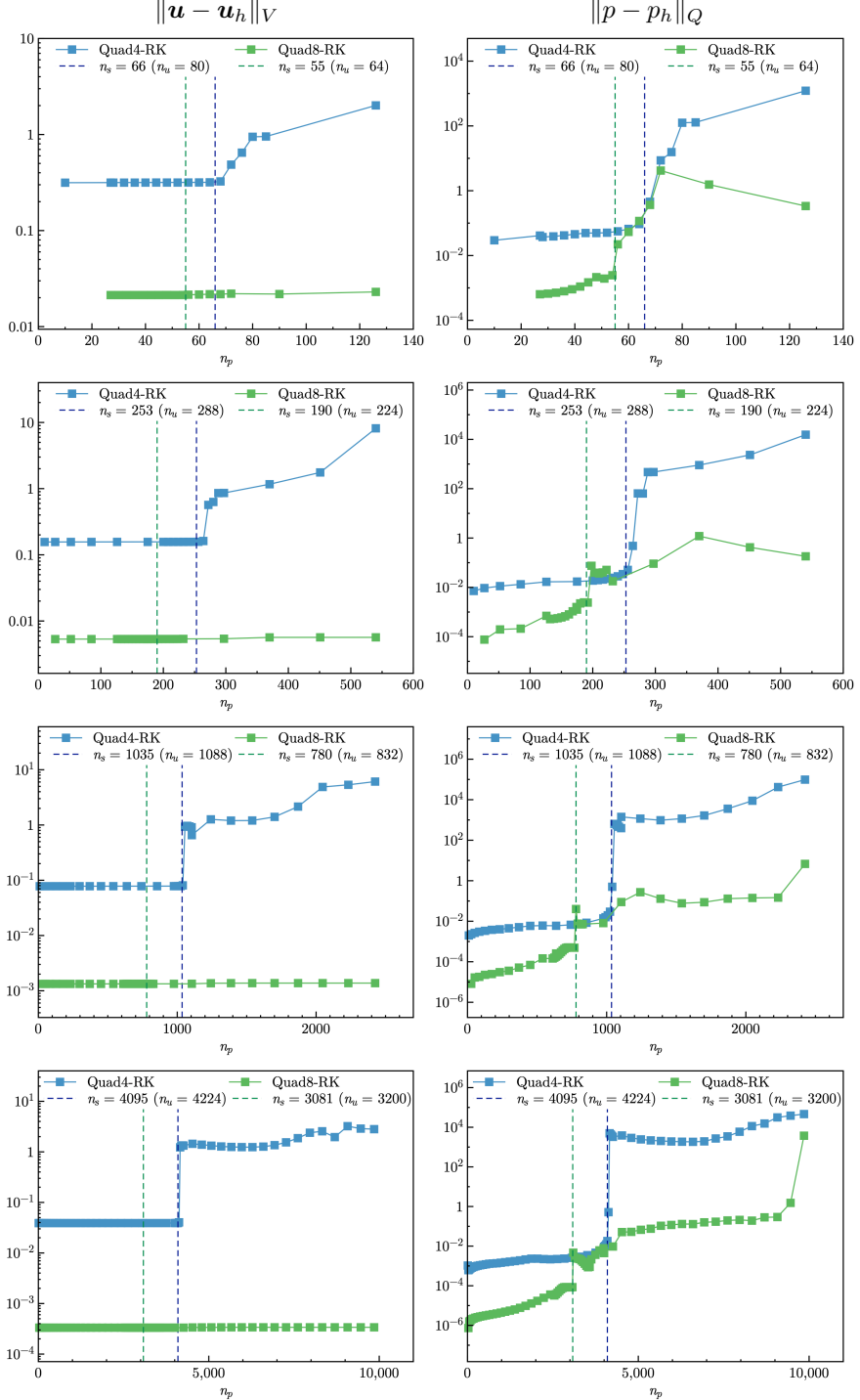


Figure 13: Strain and pressure errors vs. n_p for cantilever beam problem [with quadrilateral elements](#)

441 this context, the strain error of Eq. (A.10) is independent of the inf-sup value
 442 β and remains at a low level.

443 To further investigate the performance of proposed methods in unstructured
 444 mesh, a non-uniform discretization version of the study on strain and pressure
 445 errors with respect to n_p is conducted shown in Figure 14. Accordingly, the
 446 pressure nodes are also non-uniformly distributed and independent of the displacement
 447 nodes. The related results, shown in Figure 15, imply that all errors increase
 448 more rapidly as the constraint ratio falls outside the optimal range. The quadratic
 449 approximations, Tri6-RK and Quad8-RK, demonstrate better performance in
 450 resisting volumetric locking. In this case, the increase in Tri6-RK's strain and
 451 pressure errors has a gentler slope when the number of pressure nodes exceeds
 452 n_s .

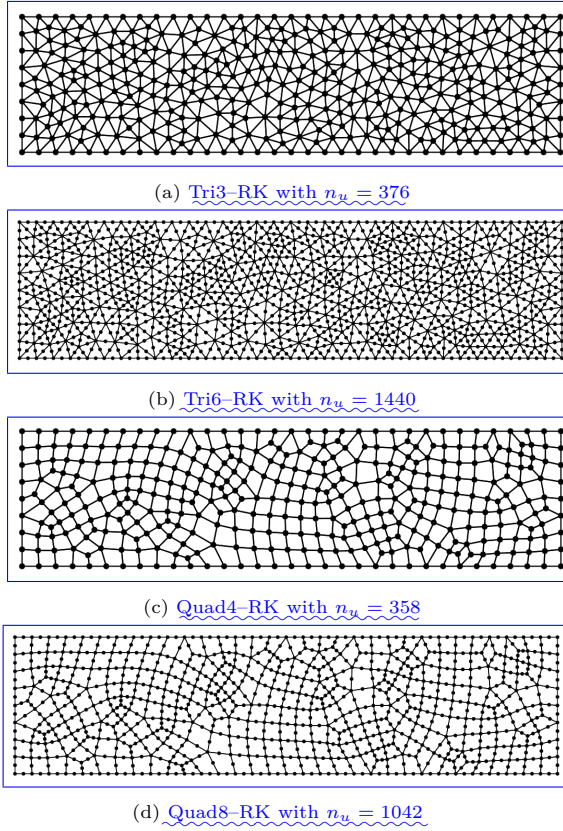


Figure 14: Non-uniform discretizations for cantilever beam problem

453 Figures 16, 17 are the strain and pressure error convergence studies for
 454 triangular and quadrilateral elements, respectively, in which Tri3-RK, Tri6-RK
 455 with $r = n_d$, the MINI element [32], 6-node triangular displacement element
 456 with 3node continuous triangular pressure element (T6C3) are the comparative

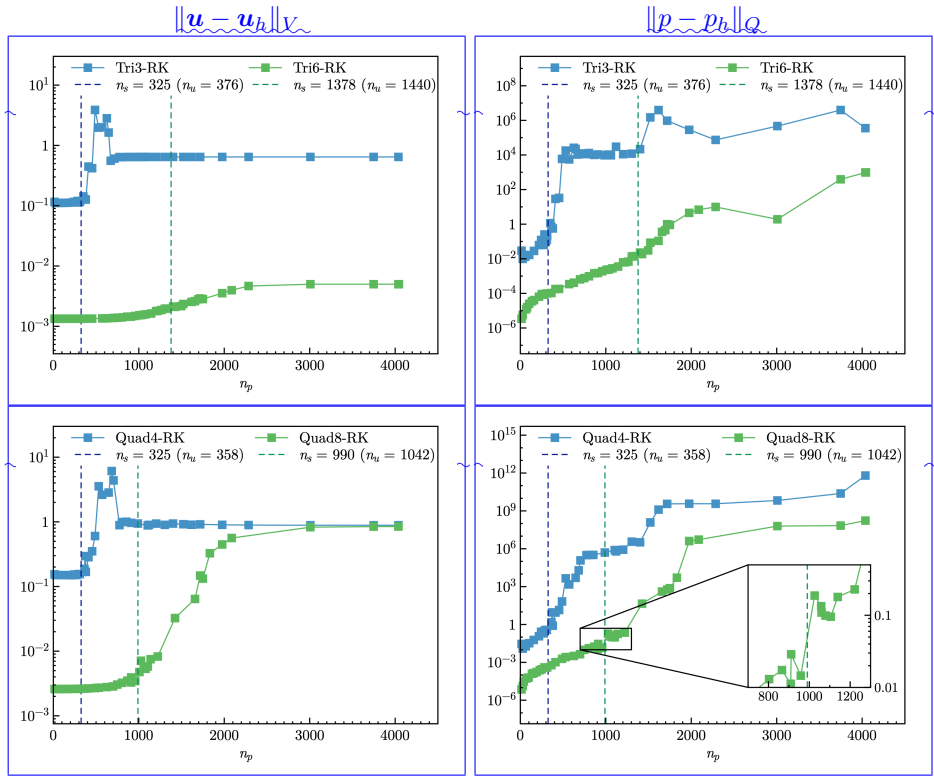


Figure 15: Strain and pressure errors vs. n_p for cantilever beam problem with non-uniform discretizations

457 methods for Tri3–RK and Tri6–RK with $r = r_{opt}$, and Quad4–RK, Quad8–RK
 458 with $r = n_d$, 4-node quadrilateral displacement element with 1-node piece-
 459 wise constant pressure (Q4P1), 8-node quadrilateral displacement element with
 460 3-node piecewise linear pressure (Q8P3) are employed for comparison with
 461 Quad4–RK and Quad8–RK with $r = r_{opt}$. Except Tri3–RK, Quad8–RK with
 462 $r = n_d$ for strain error, all formulations with the traditional constraint ratio of
 463 $r = n_d$ cannot ensure the optimal error convergence rates. The proposed mixed
 464 formulations with $r = r_{opt}$ can maintain the optimal error convergence ratio,
 465 except the strain error of Quad8–RK is a little larger than that of Q8P3, the
 466 proposed approaches show the best performance in accuracy.

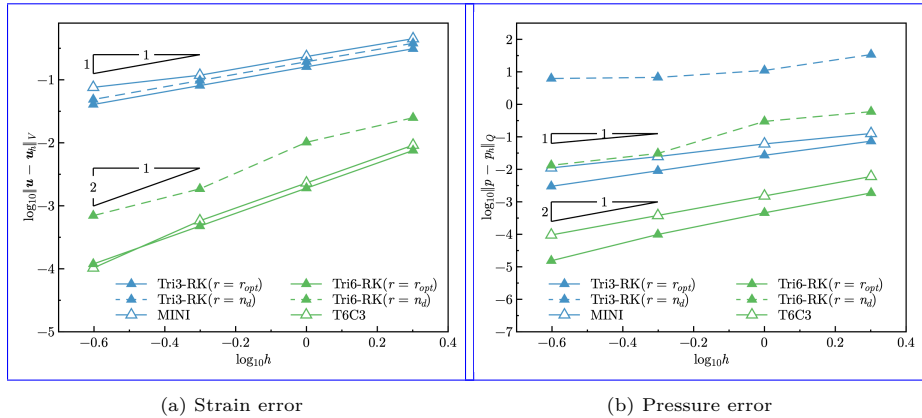


Figure 16: Error convergence study for cantilever beam problem with triangular elements

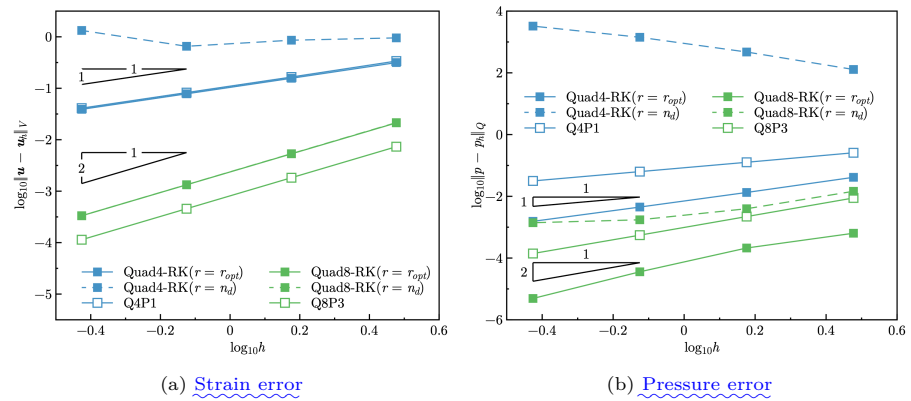


Figure 17: Error convergence study for cantilever beam problem with quadrilateral elements

467 5.2. Plate with hole problem

468 Consider an infinite plate with a hole centered at the origin, as shown in
 469 Figure 18, and at the infinity towards the x -direction subjected to a uniform

⁴⁷⁰ traction $T = 1000$. The geometric and material parameters for this problem are
⁴⁷¹ that the ratio of the hole $a = 1$, Young's modulus $E = 3 \times 10^6$, and Poisson's
⁴⁷² ratio $\nu = 0.5 - 10^{-8}$. The analytical solution of this problem refers to the
⁴⁷³ Michell solution [61] as:

$$\begin{cases} u_x(\rho, \theta) = \frac{Ta}{8\mu} \left(\frac{\rho}{a}(k+1) \cos \theta - \frac{2a^3}{\rho^3} \cos 3\theta + \frac{2a}{\rho} ((1+k) \cos \theta + \cos 3\theta) \right) \\ u_y(\rho, \theta) = \frac{Ta}{8\mu} \left(\frac{\rho}{a}(k-3) \sin \theta - \frac{2a^3}{\rho^3} \sin 3\theta + \frac{2a}{\rho} ((1-k) \sin \theta + \sin 3\theta) \right) \end{cases} \quad (63)$$

⁴⁷⁴ in which $k = \frac{3-\nu}{1+\nu}$, $\mu = \frac{E}{2(1+\nu)}$. And the stress components are given by:

$$\begin{cases} \sigma_{xx} = T \left(1 - \frac{a^2}{\rho^2} \left(\frac{3}{2} \cos 2\theta + \cos 4\theta \right) + \frac{3a^4}{2\rho^4} \cos 4\theta \right) \\ \sigma_{yy} = -T \left(\frac{a^2}{\rho^2} \left(\frac{1}{2} \cos 2\theta - \cos 4\theta \right) + \frac{3a^4}{2\rho^4} \cos 4\theta \right) \\ \sigma_{xy} = -T \left(\frac{a^2}{\rho^2} \left(\frac{1}{2} \sin 2\theta + \sin 4\theta \right) - \frac{3a^4}{2\rho^4} \sin 4\theta \right) \end{cases} \quad (64)$$

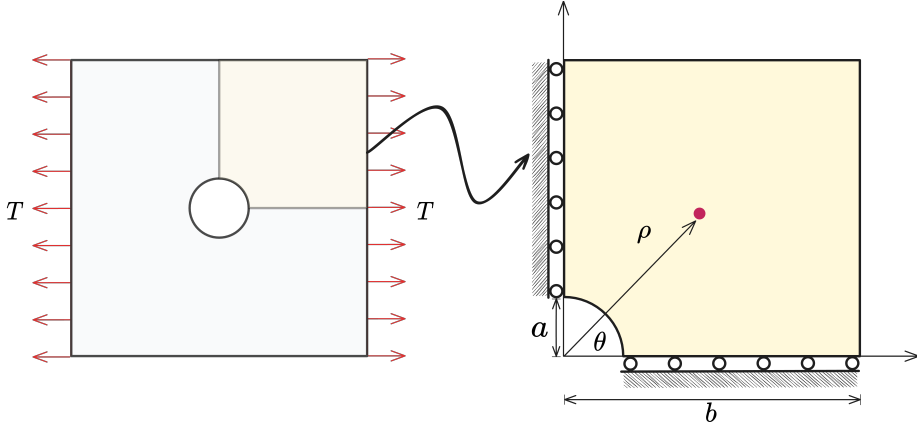


Figure 18: Illustration of plate with hole problem

⁴⁷⁵ According to the symmetry property of this problem, only a quarter model
⁴⁷⁶ with length $b = 5$ is considered as shown in Figure 18. The displacement is dis-
⁴⁷⁷ cretized by 3-node, 6-node triangular elements, 4-node and 8-node quadrilateral
⁴⁷⁸ elements. The corresponding linear and quadratic meshfree formulations are em-
⁴⁷⁹ployed for pressure discretization, and the characterized support sizes are cho-
⁴⁸⁰sen as 1.5 and 2.5, respectively. Figures 19, 20 study the relationship between
⁴⁸¹strain, pressure errors, and n_p using the nodal distributions uniformly related
⁴⁸²to displacement nodes. Unlike the quadrilateral element case in Section 5.1,
⁴⁸³both displacement and pressure errors in this problem increase as n_p reduces

484 to a small value. Tri3-RK exhibits less sensitivity in strain error than Tri6-
 485 RK. This is because, as shown in Eqs. (A.10) and (A.20), the displacement
 486 approximation error for the space of $\ker \mathcal{P}_h$ does not increase as immediately
 487 when $\frac{C_p}{\rho}$ in Eq. (A.20) is not too much larger than 1. However, its error
 488 increases as n_p goes up. Both FE-RK with constraint ratios under the optimal
 489 range perform acceptably.

490 The corresponding error convergence studies are presented in Figures 21,
 491 22, the results show that only Tri3-RK with $r = 2$ shows a comparable strain
 492 error with the optimal one with $r = r_{opt}$ in strain error. The other formulations
 493 with the traditional constraint ratio show lower accuracy and error convergence
 494 rates.

495 Furthermore, the influence of the integration scheme for this problem is
 496 investigated. As shown in Tables 4 and 5, the integration order n_o is varied
 497 from 1 to 5 for triangular elements and from 1 to 11 for quadrilateral elements.
 498 The results show that the proposed mixed formulations are not sensitive to the
 499 integration order. Using the traditional lower-order Gauss integration scheme
 500 can sufficiently obtain accurate results. This is consistent with the previous
 501 analysis in Section 4.1.

Table 4: Error comparison with different triangular integration schemes for plate with hole problem

n_o	n_g for Ω	n_g for Γ	Tri3-RK		Tri6-RK	
			$\ \mathbf{u} - \mathbf{u}_h\ _V$	$\ \mathbf{p} - \mathbf{p}_h\ _Q$	$\ \mathbf{u} - \mathbf{u}_h\ _V$	$\ \mathbf{p} - \mathbf{p}_h\ _Q$
1	1	1	3.11E-2	3.53E-3	8.53E17	1.31E4
2	3	2	3.11E-2	3.67E-3	8.33E-3	1.20E-3
3	4	2	3.11E-2	3.67E-3	8.32E-3	1.20E-3
4	6	3	3.11E-2	3.68E-3	8.32E-3	1.22E-3
5	7	3	3.11E-2	3.68E-3	8.32E-3	1.22E-3

n_o : Integration order n_g : Number of integration points

5.3. Cook's membrane problem

503 The Cook's membrane problem [12] is used herein for stability analysis of
 504 pressure. The geometry of this problem is shown in Figure 23, in which the left
 505 hand side is fixed and the right hand side subjects a concentrated force $P = 6.25$
 506 in the y -direction. The material parameters are Young's modulus $E = 70.0$ and
 507 Poisson's ratio $\nu = 0.5 - 10^{-8}$.

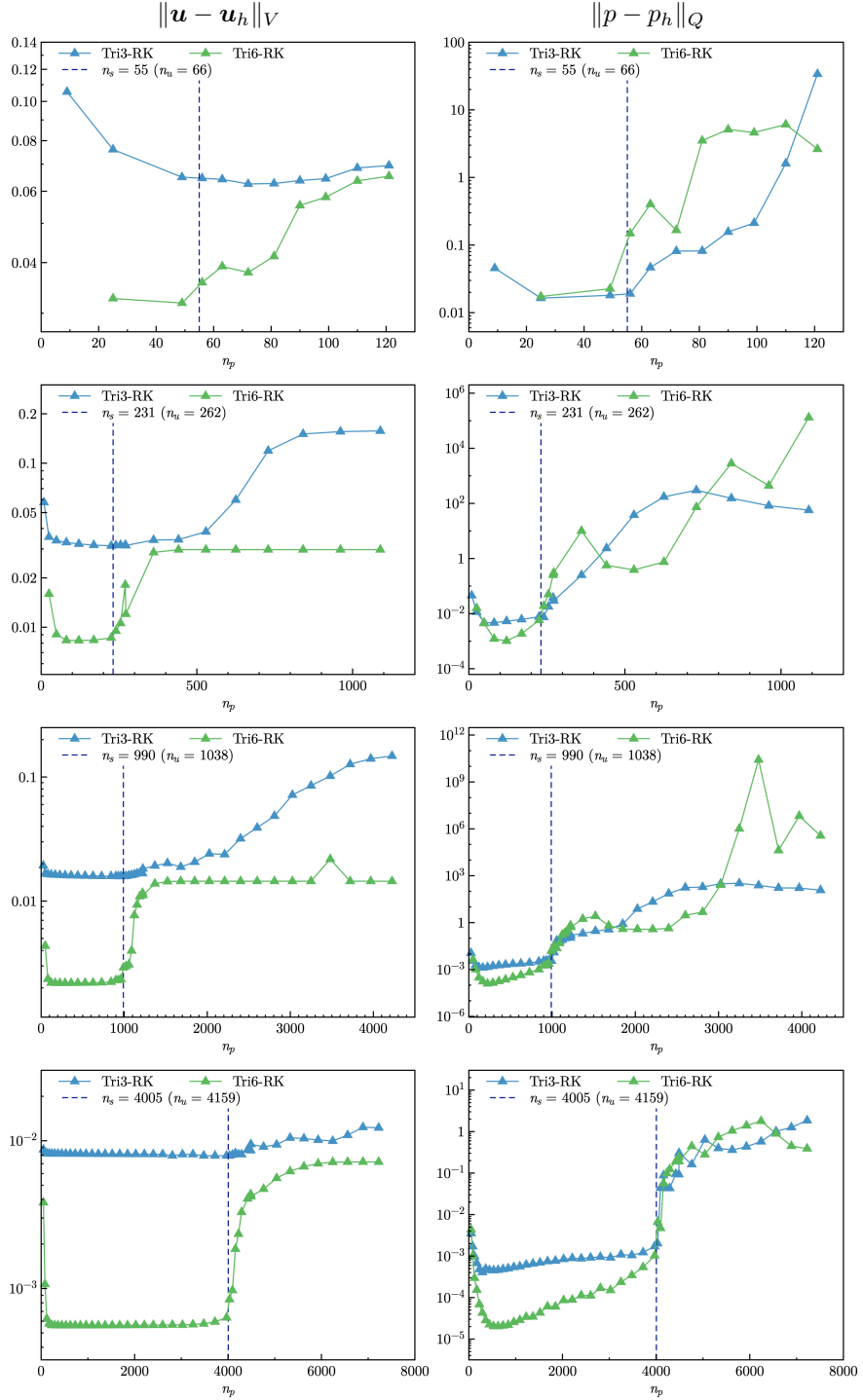


Figure 19: Strain and pressure errors vs. n_p for plate with hole problem [with triangular elements](#)

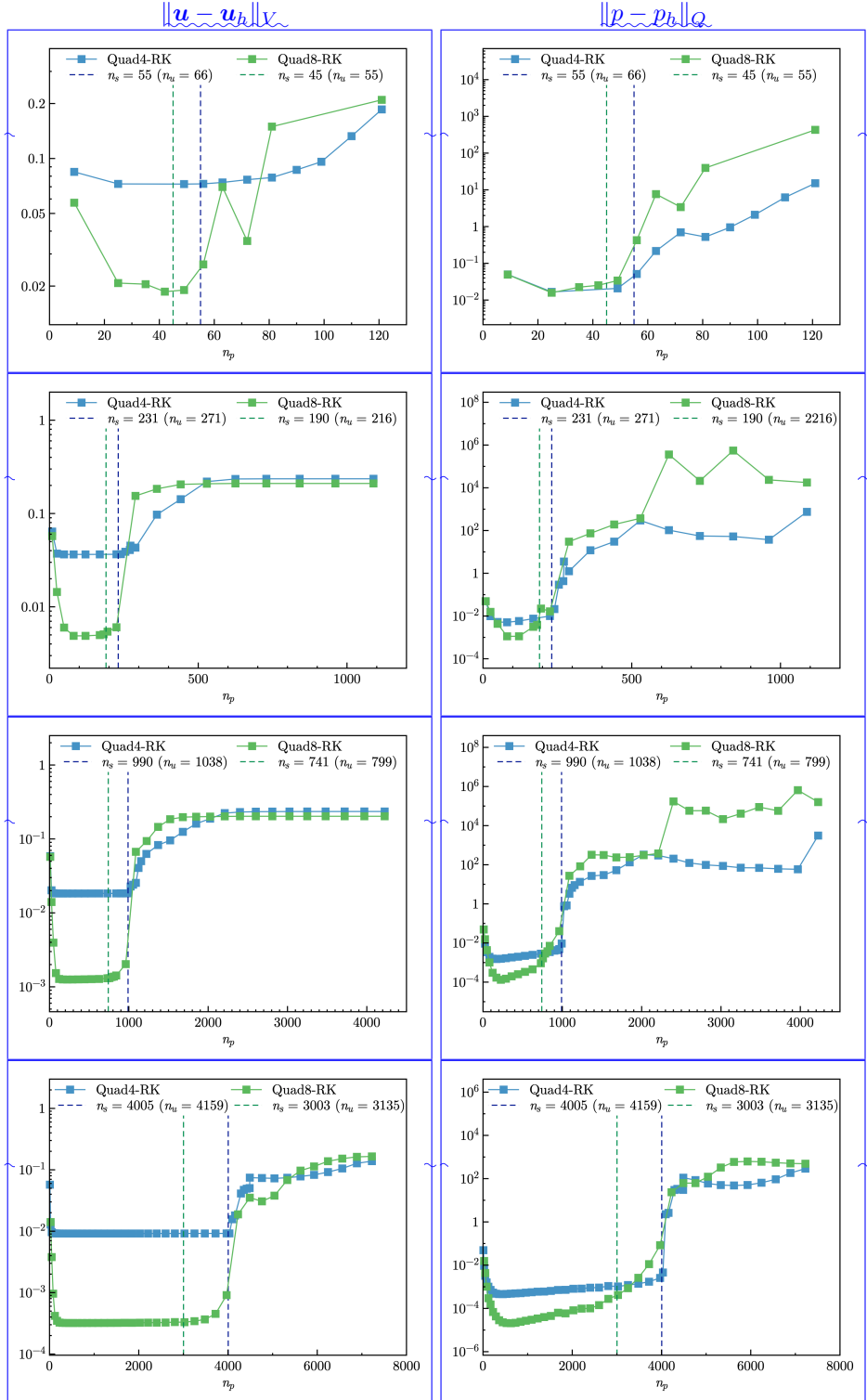


Figure 20: Strain and pressure errors vs. n_p for plate with hole problem with quadrilateral elements

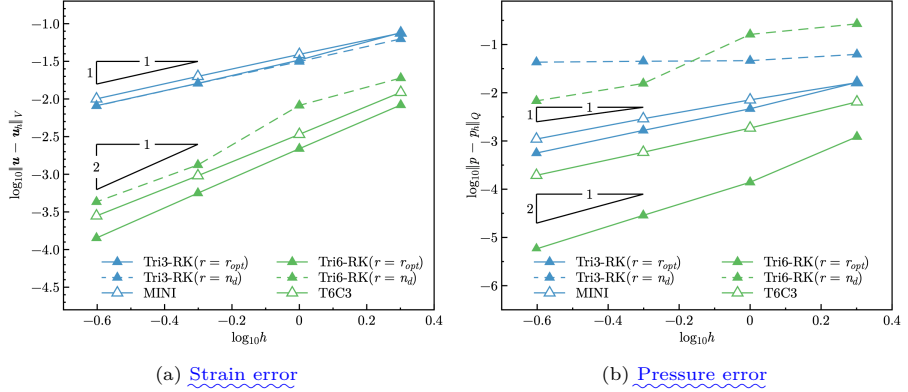


Figure 21: Error convergence study for plate with hole problem with triangular elements

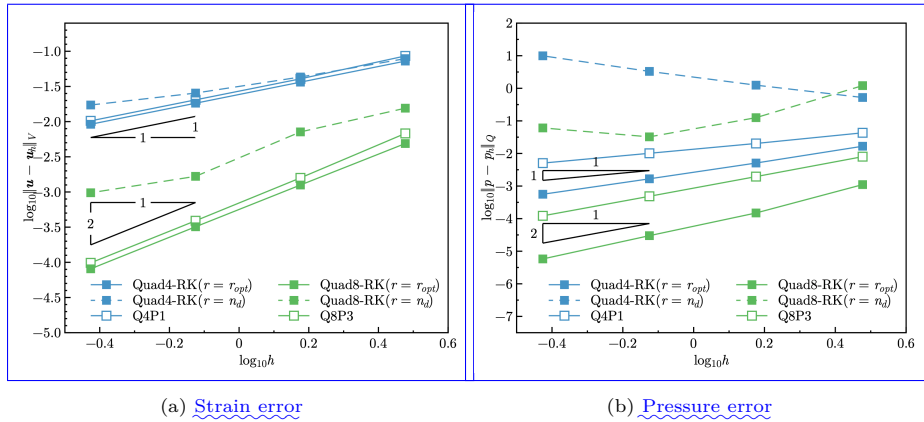


Figure 22: Error convergence study for plate with hole problem with quadrilateral elements

Table 5: Error comparison with different quadrilateral integration schemes for plate with hole problem

n_o	n_g for Ω	n_g for Γ	Quad4-RK		Quad8-RK	
			$\ u - u_b\ _V$	$\ \rho - \rho_b\ _{\Omega}$	$\ u - u_b\ _V$	$\ \rho - \rho_b\ _{\Omega}$
1	3	1	3.64E-2	5.01E-3	9.53E13	8.15E-1
3	2×2	2	3.64E-2	5.09E-3	4.33E-2	8.84E-3
5	3×3	3	3.62E-2	3.71E-3	1.27E-3	4.42E-5
7	4×4	4	3.62E-2	3.70E-3	1.26E-3	1.49E-4
9	5×5	5	3.62E-2	3.70E-3	1.26E-3	1.50E-4
11	6×6	6	3.62E-2	3.70E-3	1.26E-3	1.50E-4

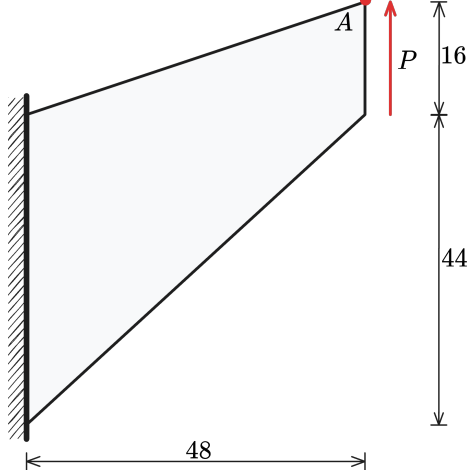


Figure 23: Illustration of Cook's membrane problem

508 In this test, we evaluated the convergence properties by comparing the vertical
 509 displacement at point A against a reference value of 28.0. As shown in
 510 Figure 24 illustrates, the methods employing $r = r_{opt}$ produced results that
 511 were notably closer to this reference value than those using $r = n_d$. Furthermore,
 512 to investigate stability, Figures 25–28 show the pressure contour plots for
 513 non-uniform Tri3–RK, Tri6–RK, Quad4–RK, and Quad8–RK formulations with
 514 $r = n_d$ and $r = r_{opt}$, respectively. The reproducing kernel meshfree approximations
 515 are employed for pressure discretization with characterized support sizes
 516 of 1.5 for the linear basis function and 2.5 for the quadratic basis function. The
 517 results imply that the pressure contour plots with the optimal constraint ratio
 518 $r = r_{opt}$ show a more stable and smooth pressure distribution compared to those
 519 with the traditional constraint ratio $r = n_d$.

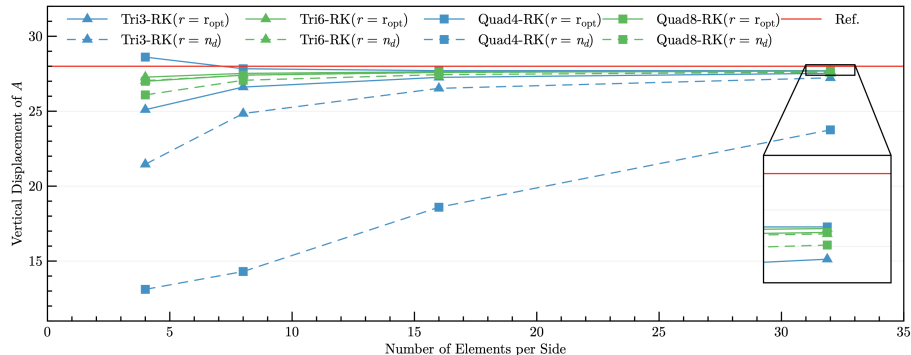


Figure 24: Convergence comparison of the vertical displacement at point A for Cook's membrane problem

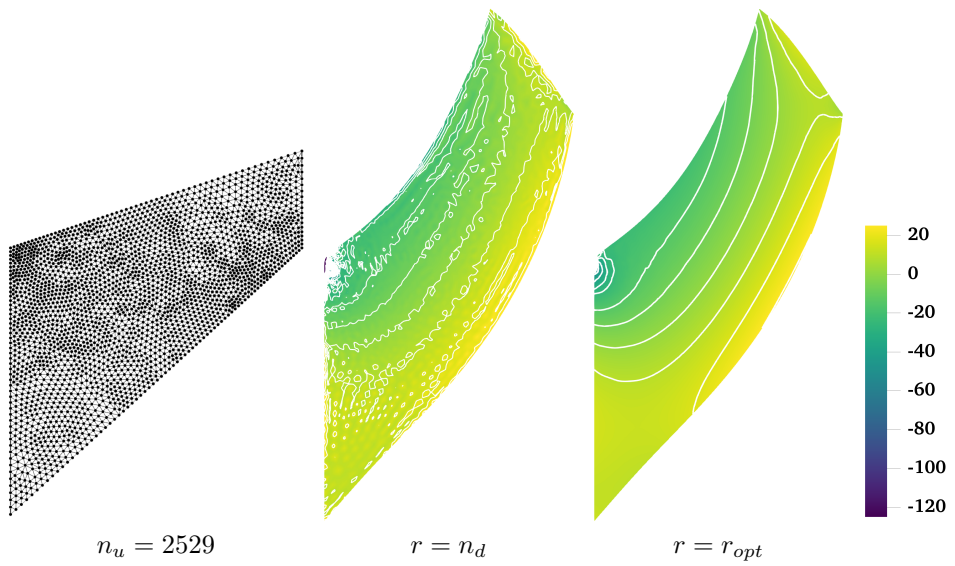


Figure 25: Pressure contour plots for Cook's membrane problem using Tri3–RK

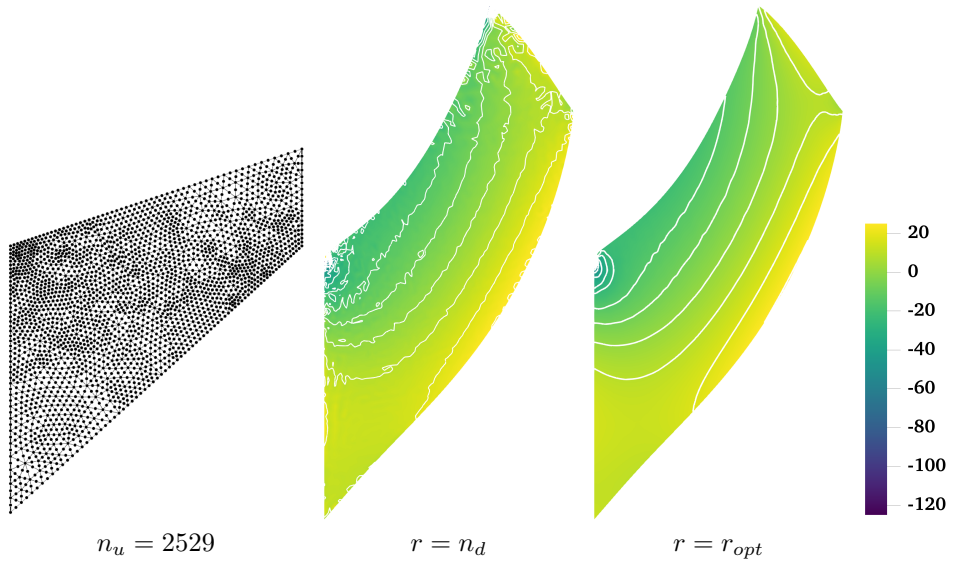


Figure 26: Comparison of pressure contour plots for Cook's membrane problem using Tri6–RK

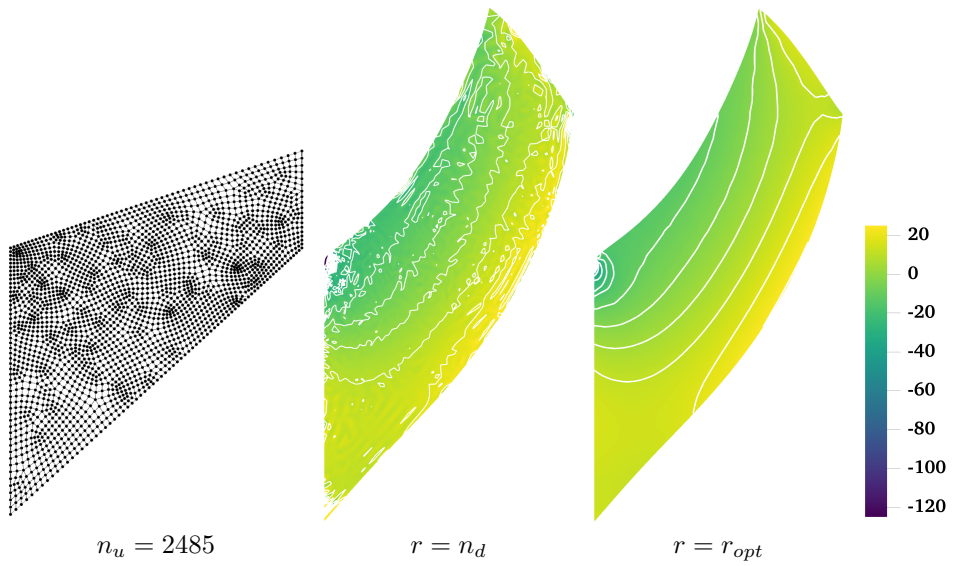


Figure 27: Comparison of pressure contour plots for Cook's membrane problem using Quad4–RK

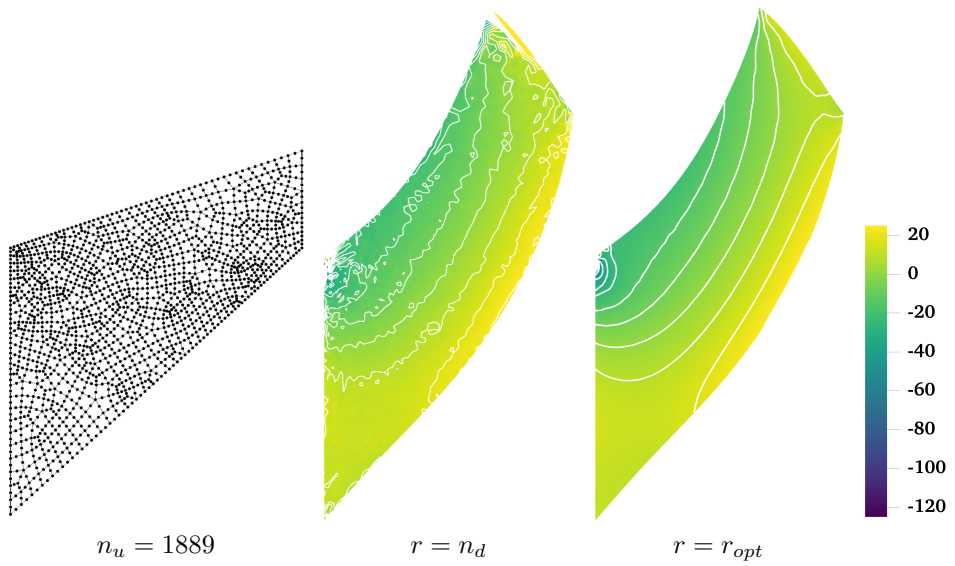


Figure 28: Comparison of pressure contour plots for Cook's membrane problem using Quad8–RK

520 An efficiency comparison of different methods for the Cook's membrane
 521 problem is presented in Table 6. This includes the condition number of the
 522 global stiffness matrix and the CPU time for shape function construction, system
 523 assembly, and system solving. The mixed FE-Meshfree formulations exhibit
 524 higher condition number and spend more time compared to the traditional
 525 element-based formulations. This is mainly due to the implicit, complicated
 526 expression of meshfree shape functions and the larger bandwidth of the stiffness
 527 matrix, which results from the larger support size of the meshfree shape functions.
 528

Table 6: Condition number and efficiency comparison for Cook's membrane problem

Method ~	Condition number ~	CPU-time (s) for			Solving
		Shape function	Assembly		
MINI	1.11E06	0.025	0.327	0.022	
Tri3-RK($r = n_d$)	1.89E10	1.730	4.160	0.108	
Tri3-RK($r = r_{opt}$)	1.13E08	1.290	1.720	0.052	
T6C3	1.62E05	0.004	0.380	0.021	
Tri6-RK($r = n_d$)	2.48E16	1.620	1.670	0.294	
Tri6-RK($r = r_{opt}$)	3.69E10	1.110	0.634	0.077	
Q4P1	5.75E12	0.011	0.344	0.021	
Quad4-RK($r = n_d$)	5.21E10	2.100	4.890	0.122	
Quad4-RK($r = r_{opt}$)	1.97E08	1.500	2.140	0.057	
Q8P3	2.69E07	0.005	0.373	0.015	
Quad8-RK($r = n_d$)	2.75E15	1.170	1.180	0.184	
Quad8-RK($r = r_{opt}$)	8.67E10	0.847	0.471	0.065	

529 5.4. Block under compression problem

530 The incompressible block problem [62] shown in Figure 29 is considered for
 531 testing 3D mixed formulations. The block's dimensions are $2L \times 2L \times L$, $L = 1$.
 532 At the center of the top surface of the block is applied a pressure load P with
 533 the area of $L \times L$. Due to the symmetry of this problem, only a quarter model is
 534 considered. The Young's modulus and Poisson's ratio are set as $E = 240.56839$
 535 and $\nu = 0.5 - 10^{-8}$, respectively.

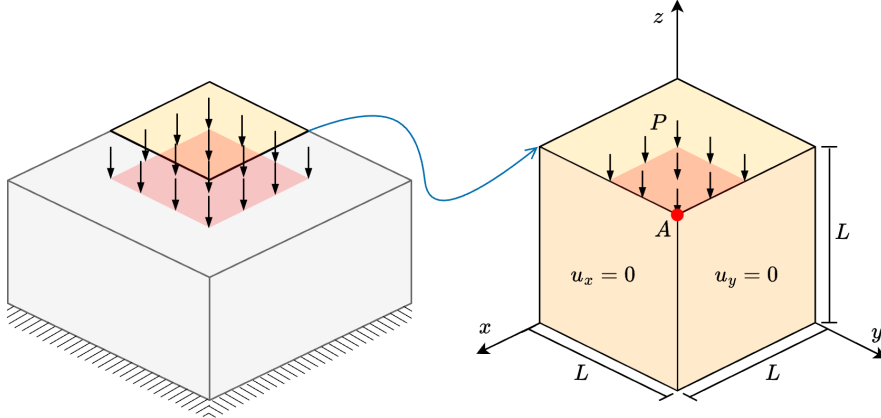


Figure 29: Illustration of block under compression problem

536 The convergence properties of the mixed formulations are evaluated by com-
 537 paring the compression level at point A under loading condition $P = 80$. The
 538 4-node tetrahedron element with the MINI scheme (Tet4-MINI) and the 8-node
 539 hexahedron element with piecewise constant pressure formulation (H8P1) are
 540 introduced herein as comparison methods. As shown in Figure 30, all the results
 541 exhibit good convergence behavior across different loading levels. Figures 31, 32
 542 study the pressure stability of 3D mixed FE-meshfree formulations, Tet4-RK
 543 and Hex8-RK, with non-uniform nodal distribution, while the pressure is dis-
 544 cretized by linear meshfree approximations with a characterized support size of
 545 1.5. The corresponding results also show the well performance of the proposed
 546 optimal constraint ratio $r = r_{opt}$. The mixed formulations with the traditional
 547 constraint ratio $r = n_d$ show comparable displacement results, but exhibit sig-
 548 nificant pressure instability.

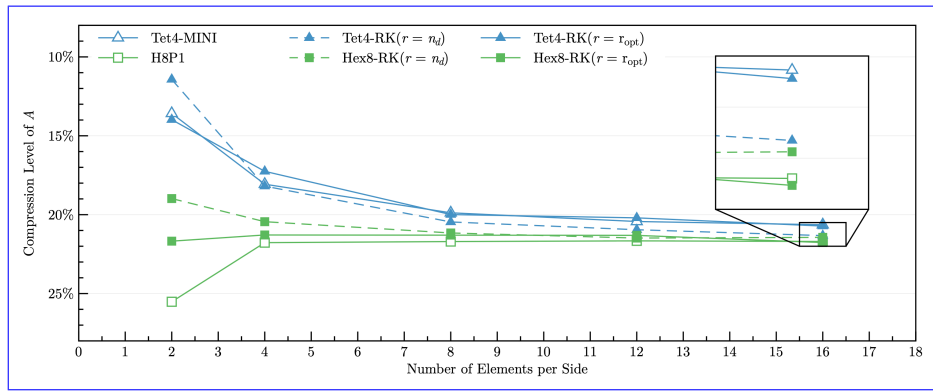


Figure 30: Convergence comparison of compression level (%) at point A for block under compression problem

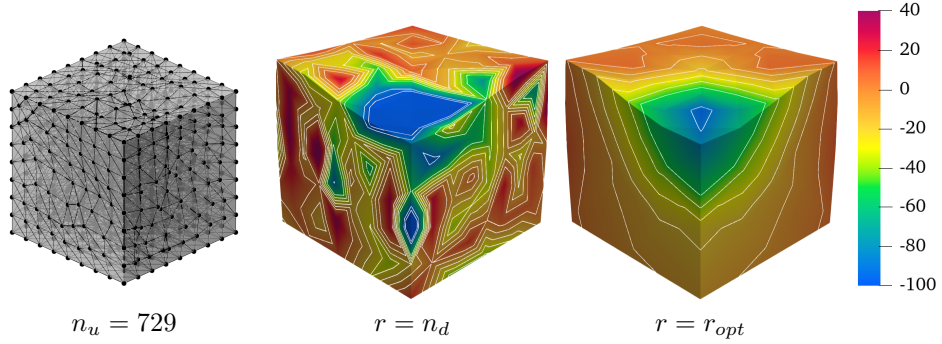


Figure 31: Comparison of pressure contour plots for block under compression problem using Tet4–RK

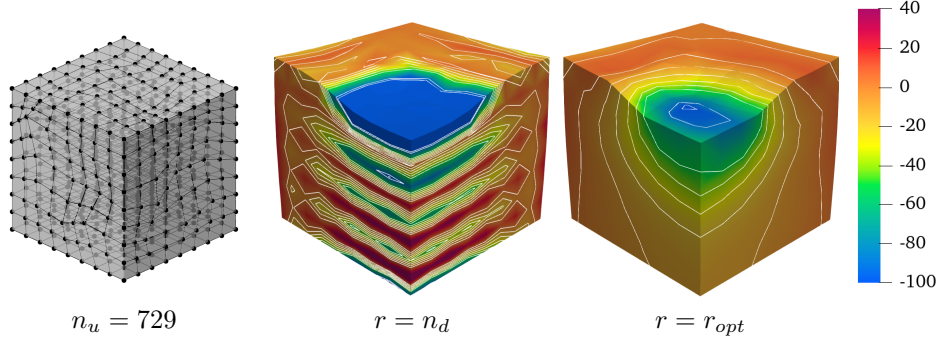


Figure 32: Comparison of pressure contour plots for block under compression problem using Hex8–RK

549 6. Conclusion

550 This paper proposes a novel optimal constraint ratio derived from the inf–sup
 551 condition to address volumetric locking. The optimal constraint ratio requires
 552 that, for a given number of displacement DOFs, the number of pressure DOFs
 553 should remain below a stabilized number determined by the proposed inf–sup
 554 value estimator. For a well-posed nodal distribution, simply counting the dis-
 555 placement and pressure DOFs can determine whether the formulation satisfies
 556 the inf–sup condition. Compared to the traditional constraint ratio, the pro-
 557 posed ratio is theoretically grounded in the inf–sup condition and thus is more
 558 precise, and it also provides a simple way, by counting the DOFs of displacement
 559 and pressure fields, to justify the satisfaction of inf–sup condition.

560 To implement this constraint ratio, a mixed finite element (FE) and meshfree
 561 formulation is developed. Displacements are discretized using 3-node and 6-
 562 node triangular elements, 4-node and 8-node quadrilateral elements in 2D, and
 563 4-node tetrahedral and 8-node hexahedral elements in 3D. Correspondingly,

564 linear and quadratic reproducing kernel meshfree approximations are used for
565 pressure discretization. The reproducing kernel approximation equips globally
566 smooth shape functions, allowing arbitrary pressure DOF placement without
567 the limit of element. However, the implicit expression of shape functions and
568 the larger bandwidth of the stiffness matrix in meshfree approximation also lead
569 to larger condition number and lower efficiency compared with traditional FE
570 formulations.

571 Inf-sup tests for mixed FE-meshfree formulations with different constraint
572 ratios verify the effectiveness of the proposed inf-sup value estimator. For effi-
573 ciency and ease of implementation, the final nodal distribution scheme selects
574 every other displacement node as a pressure node, ensuring the optimal con-
575 straint ratio and satisfying the inf-sup condition.

576 A series of 2D and 3D incompressible elasticity examples demonstrate the
577 effectiveness of the proposed mixed formulation. Results show that formulations
578 with the optimal constraint ratio yield accurate displacement and pressure solu-
579 tions. When the constraint ratio exceeds the optimal value, errors rise sharply
580 to unacceptable levels, with the 8-node quadrilateral element being the only
581 exception that maintains good displacement accuracy. Error convergence stud-
582 ies and pressure contour plots further confirm that mixed formulations with
583 the optimal constraint ratio achieve optimal convergence rates and effectively
584 suppress pressure oscillations.

585 Acknowledgment

586 The support of this work by the National Natural Science Foundation of
587 China (12102138), the Natural Science Foundation of Fujian Province of China
588 (2023J01108) and the Fundamental Research Funds of Central Universities
589 (ZQN-1014) is gratefully acknowledged.

590 References

- 591 [1] F. Brezzi, M. Fortin, Mixed and Hybrid Finite Element Methods, Vol. 15 of
592 Springer Series in Computational Mathematics, Springer, New York, NY,
593 1991.
- 594 [2] T. J. Hughes, The Finite Element Method: Linear Static and Dynamic
595 Finite Element Analysis, Prentice Hall, New Jersey, 2000.
- 596 [3] I. Babuška, R. Narasimhan, The Babuška-Brezzi condition and the patch
597 test: An example, Computer Methods in Applied Mechanics and Engineering
598 140 (1-2) (1997) 183–199.
- 599 [4] K. J. Bathe, Finite Element Procedures, Prentice Hall, Englewood Cliffs,
600 New Jersey, 1996.
- 601 [5] D. S. Malkus, Eigenproblems associated with the discrete LBB condition for
602 incompressible finite elements, International Journal of Engineering Science
603 19 (10) (1981) 1299–1310.

- 604 [6] D. Chapelle, K. J. Bathe, The inf-sup test, Computers & Structures 47 (4)
 605 (1993) 537–545.
- 606 [7] F. Brezzi, K. J. Bathe, Studies of finite element procedures the inf-sup
 607 condition equivalent forms and applications.
- 608 [8] D. Gallistl, Rayleigh-Ritz approximation of the inf-sup constant for the
 609 divergence, Mathematics of Computation 88 (315) (2019) 73–89.
- 610 [9] P. Hood, C. Taylor, Navier-Stokes equations using mixed interpolation,
 611 Finite element methods in flow problems (1974) 121–132.
- 612 [10] D. S. Malkus, T. J. Hughes, Mixed finite element methods - Reduced and
 613 selective integration techniques: A unification of concepts, Computer Meth-
 614 ods in Applied Mechanics and Engineering 15 (1) (1978) 63–81.
- 615 [11] T. Shilt, R. Deshmukh, J. J. McNamara, P. J. O'Hara, Solution of nearly
 616 incompressible field problems using a generalized finite element approach,
 617 Computer Methods in Applied Mechanics and Engineering 368 (2020)
 618 113165.
- 619 [12] J. C. Simo, M. S. Rifai, A class of mixed assumed strain methods and
 620 the method of incompatible modes, International Journal for Numerical
 621 Methods in Engineering 29 (8) (1990) 1595–1638.
- 622 [13] M. Broccardo, M. Micheloni, P. Krysl, Assumed-deformation gradient finite
 623 elements with nodal integration for nearly incompressible large deformation
 624 analysis, International Journal for Numerical Methods in Engineering 78 (9)
 625 (2009) 1113–1134.
- 626 [14] W. M. Coombs, T. J. Charlton, M. Cortis, C. E. Augarde, Overcoming vol-
 627 umetric locking in material point methods, Computer Methods in Applied
 628 Mechanics and Engineering 333 (2018) 1–21.
- 629 [15] S. Saloustros, M. Cervera, S. Kim, M. Chiumenti, Accurate and locking-free
 630 analysis of beams, plates and shells using solid elements, Computational
 631 Mechanics 67 (2021) 883–914.
- 632 [16] J. Simo, R. Taylor, K. Pister, Variational and projection methods for the
 633 volume constraint in finite deformation elasto-plasticity, Computer Meth-
 634 ods in Applied Mechanics and Engineering 51 (1-3) (1985) 177–208.
- 635 [17] C. R. Dohrmann, P. B. Bochev, A stabilized finite element method for the
 636 Stokes problem based on polynomial pressure projections, International
 637 Journal for Numerical Methods in Fluids 46 (2) (2004) 183–201.
- 638 [18] A. Valverde-González, J. Reinoso, B. Dortdivanlioglu, M. Paggi, Locking
 639 treatment of penalty-based gradient-enhanced damage formulation for fail-
 640 ure of compressible and nearly incompressible hyperelastic materials, Com-
 641 putational Mechanics 72 (2023) 635–662.

- 642 [19] B.-B. Xu, F. Peng, P. Wriggers, Stabilization-free virtual element method
 643 for finite strain applications, Computer Methods in Applied Mechanics and
 644 Engineering 417 (2023) 116555.
- 645 [20] F. S. Liguori, A. Madeo, S. Marfia, G. Garcea, E. Sacco, A stabilization-
 646 free hybrid virtual element formulation for the accurate analysis of 2D
 647 elasto-plastic problems, Computer Methods in Applied Mechanics and En-
 648 gineering 431 (2024) 117281.
- 649 [21] R. Alves de Sousa, R. Natal Jorge, R. Fontes Valente, J. César de Sá, A new
 650 volumetric and shear locking-free 3D enhanced strain element, Engineering
 651 Computations 20 (7) (2003) 896–925.
- 652 [22] K.-J. Bathe, The inf-sup condition and its evaluation for mixed finite ele-
 653 ment methods, Computers & Structures 79 (2) (2001) 243–252.
- 654 [23] T. J. R. Hughes, Multiscale phenomena: Green's functions, the Dirichlet-
 655 to-Neumann formulation, subgrid scale models, bubbles and the origins of
 656 stabilized methods, Computer Methods in Applied Mechanics and Engi-
 657 neering 127 (1) (1995) 387–401.
- 658 [24] R. Rossi, R. Zorrilla, R. Codina, A stabilised displacement-volumetric
 659 strain formulation for nearly incompressible and anisotropic materials,
 660 Computer Methods in Applied Mechanics and Engineering 377 (2021)
 661 113701.
- 662 [25] E. Karabelas, M. A. F. Gsell, G. Haase, G. Plank, C. M. Augustin, An
 663 accurate, robust, and efficient finite element framework with applications to
 664 anisotropic, nearly and fully incompressible elasticity, Computer Methods
 665 in Applied Mechanics and Engineering 394 (2022) 114887.
- 666 [26] R. Codina, I. Castañar, J. Baiges, Finite element approximation of stabi-
 667 lized mixed models in finite strain hyperelasticity involving displace-
 668 ments and stresses and/or pressure—An overview of alternatives, International
 669 Journal for Numerical Methods in Engineering (2024) e7540.
- 670 [27] L. Moreno, R. Wuechner, A. Larese, A mixed stabilized MPM formula-
 671 tion for incompressible hyperelastic materials using Variational Subgrid-
 672 Scales, Computer Methods in Applied Mechanics and Engineering 435
 673 (2025) 117621.
- 674 [28] T. J. R. Hughes, L. P. Franca, M. Balestra, A new finite element formu-
 675 lation for computational fluid dynamics: V. Circumventing the babuška-
 676 brezzi condition: A stable Petrov-Galerkin formulation of the stokes prob-
 677 lem accommodating equal-order interpolations, Computer Methods in Ap-
 678 plied Mechanics and Engineering 59 (1) (1986) 85–99.
- 679 [29] A. N. Brooks, T. J. R. Hughes, Streamline upwind/Petrov-Galerkin formu-
 680 lations for convection dominated flows with particular emphasis on the in-
 681 compressible Navier-Stokes equations, Computer Methods in Applied Me-
 682 chanics and Engineering 32 (1) (1982) 199–259.

- 683 [30] L. He, L. Jing, M. Feng, New stabilized mixed finite element methods for
 684 two-field poroelasticity with low permeability, *Applied Mathematics and*
 685 *Computation* 494 (2025) 129285.
- 686 [31] D. N. Arnold, F. Brezzi, M. Fortin, A stable finite element for the Stokes
 687 equations, *CALCOLO* 21 (4) (1984) 337–344.
- 688 [32] F. Auricchio, L. Beirão da Veiga, C. Lovadina, A. Reali, A stability study of
 689 some mixed finite elements for large deformation elasticity problems, *Com-*
 690 *puter Methods in Applied Mechanics and Engineering* 194 (9-11) (2005)
 691 1075–1092.
- 692 [33] A. Quarteroni, A. Valli, *Numerical Approximation of Partial Differen-*
 693 *tial Equations*, Springer Series in Computational Mathematics, Springer,
 694 Berlin, 1994.
- 695 [34] M. Crouzeix, P. Raviart, Conforming and nonconforming finite ele-
 696 ment methods for solving the stationary Stokes equations I, *Revue*
 697 *française d'automatique informatique recherche opérationnelle. Mathéma-*
 698 *tique* 7 (R3) (1973) 33–75.
- 699 [35] U. Brink, E. Stein, On some mixed finite element methods for incompres-
 700 sible and nearly incompressible finite elasticity, *Computational Mechanics*
 701 19 (1) (1996) 105–119.
- 702 [36] T. Belytschko, Y. Y. Lu, L. Gu, Element-free Galerkin methods, *Internation-*
 703 *al Journal for Numerical Methods in Engineering* 37 (2) (1994) 229–256.
- 704 [37] W. K. Liu, S. Jun, Y. F. Zhang, Reproducing kernel particle methods, *Internation-*
 705 *al Journal for Numerical Methods in Fluids* 20 (8-9) (1995) 1081–
 706 1106.
- 707 [38] C. Rodriguez, T.-H. Huang, A variationally consistent reproducing ker-
 708 nel enhanced material point method and its applications to incompressible
 709 materials, *Computational Mechanics* (2023) 1–20.
- 710 [39] S. W. Chi, J. S. Chen, H. Y. Hu, A weighted collocation on the strong form
 711 with mixed radial basis approximations for incompressible linear elasticity,
 712 *Computational Mechanics* 53 (2) (2014) 309–324.
- 713 [40] L. Wang, Z. Qian, Y. Zhou, Y. Peng, A weighted meshfree collocation
 714 method for incompressible flows using radial basis functions, *Journal of*
 715 *Computational Physics* 401 (2020) 108964.
- 716 [41] A. Ortiz-Bernardin, M. Puso, N. Sukumar, Improved robustness for nearly-
 717 incompressible large deformation meshfree simulations on Delaunay tes-
 718 sellations, *Computer Methods in Applied Mechanics and Engineering* 293
 719 (2015) 348–374.

- 720 [42] T. J. Hughes, J. A. Cottrell, Y. Bazilevs, Isogeometric analysis: CAD,
 721 finite elements, NURBS, exact geometry and mesh refinement, Computer
 722 Methods in Applied Mechanics and Engineering 194 (39-41) (2005) 4135–
 723 4195.
- 724 [43] F. Auricchio, L. Beirão da Veiga, C. Lovadina, A. Reali, The importance
 725 of the exact satisfaction of the incompressibility constraint in nonlinear
 726 elasticity: Mixed FEMs versus NURBS-based approximations, Computer
 727 Methods in Applied Mechanics and Engineering 199 (5) (2010) 314–323.
- 728 [44] A. Huerta, S. Fernández-Méndez, Locking in the incompressible limit for
 729 the element-free Galerkin method, International Journal for Numerical
 730 Methods in Engineering 51 (11) (2001) 1361–1383.
- 731 [45] J. Dolbow, T. Belytschko, Volumetric locking in the element free Galerkin
 732 method, International Journal for Numerical Methods in Engineering 46 (6)
 733 (1999) 925–942.
- 734 [46] G. Moutsanidis, J. J. Koester, M. R. Tupek, J.-S. Chen, Y. Bazilevs, Treat-
 735 ment of near-incompressibility in meshfree and immersed-particle methods,
 736 Computational Particle Mechanics 7 (2) (2020) 309–327.
- 737 [47] G. Moutsanidis, W. Li, Y. Bazilevs, Reduced quadrature for FEM, IGA
 738 and meshfree methods, Computer Methods in Applied Mechanics and En-
 739 gineering 373 (2021) 113521.
- 740 [48] Z.-Y. Wang, Y.-F. Jin, Z.-Y. Yin, Y.-Z. Wang, Overcoming volumetric
 741 locking in stable node-based smoothed particle finite element method with
 742 cubic bubble function and selective integration, International Journal for
 743 Numerical Methods in Engineering 123 (24) (2022) 6148–6169.
- 744 [49] T. Elguedj, Y. Bazilevs, V. Calo, T. Hughes, B[−] and F[−] projection meth-
 745 ods for nearly incompressible linear and non-linear elasticity and plasticity
 746 using higher-order NURBS elements, Computer Methods in Applied Me-
 747 chanics and Engineering 197 (33-40) (2008) 2732–2762.
- 748 [50] J. S. Chen, S. Yoon, H. P. Wang, W. K. Liu, An improved reproducing
 749 kernel particle method for nearly incompressible finite elasticity, Computer
 750 Methods in Applied Mechanics and Engineering 181 (1) (2000) 117–145.
- 751 [51] C. M. Goh, P. M. F. Nielsen, M. P. Nash, A stabilised mixed mesh-
 752 free method for incompressible media: Application to linear elasticity and
 753 Stokes flow, Computer Methods in Applied Mechanics and Engineering 329
 754 (2018) 575–598.
- 755 [52] D. S. Bombarde, M. Agrawal, S. S. Gautam, A. Nandy, Hellinger–Reissner
 756 principle based stress–displacement formulation for three-dimensional iso-
 757 geometric analysis in linear elasticity, Computer Methods in Applied Me-
 758 chanics and Engineering 394 (2022) 114920.

- 759 [53] H. Casquero, M. Golestanian, Vanquishing volumetric locking in quadratic
 760 NURBS-based discretizations of nearly-incompressible linear elasticity:
 761 CAS elements, *Computational Mechanics* 73 (6) (2024) 1241–1252.
- 762 [54] A. Huerta, Y. Vidal, P. Villon, Pseudo-divergence-free element free
 763 Galerkin method for incompressible fluid flow, *Computer Methods in Applied
 764 Mechanics and Engineering* 193 (12-14) (2004) 1119–1136.
- 765 [55] C. T. Wu, W. Hu, J. S. Chen, A meshfree-enriched finite element method
 766 for compressible and near-incompressible elasticity, *International Journal
 767 for Numerical Methods in Engineering* 90 (7) (2012) 882–914.
- 768 [56] T. Vu-Huu, C. Le-Thanh, H. Nguyen-Xuan, M. Abdel-Wahab, A high-
 769 order mixed polygonal finite element for incompressible Stokes flow analy-
 770 sis, *Computer Methods in Applied Mechanics and Engineering* 356 (2019)
 771 175–198.
- 772 [57] E. Stein, R. de Borst, T. J. R. Hughes (Eds.), *Encyclopedia of Computational
 773 Mechanics*, John Wiley, Chichester, West Sussex, 2004.
- 774 [58] I. Babuška, J. Osborn, Eigenvalue Problems, in: *Handbook of Numerical
 775 Analysis*, Vol. 2 of *Finite Element Methods (Part 1)*, Elsevier, 1991, pp.
 776 641–787.
- 777 [59] K. Yosida, *Functional Analysis*, 6th Edition, Classics in Mathematics,
 778 Springer-Verlag, Berlin Heidelberg, 1995.
- 779 [60] J. Wu, D. Wang, An accuracy analysis of Galerkin meshfree methods ac-
 780 counting for numerical integration, *Computer Methods in Applied Mechan-
 781 ics and Engineering* 375 (2021) 113631.
- 782 [61] S. Timoshenko, J. Goodier, *Theory of Elasticity*, Engineering Mechanics
 783 Series, McGraw-Hill, 1969.
- 784 [62] S. Reese, P. Wriggers, B. D. Reddy, A new locking-free brick element tech-
 785 nique for large deformation problems in elasticity, *Computers & Structures*
 786 75 (3) (2000) 291–304.
- 787 [63] [S. C. Brenner, L. R. Scott, *The Mathematical Theory of Finite Element
 788 Methods*, Springer, New York, 2008.](#)

789 **Appendix A. Error estimator for mixed-formulation**

790 In this appendix, the traditional error estimators for mixed-formulation are
 791 illustrated herein, the proof is referred to [63]. For incompressible elasticity
 792 problems, i.e. $\kappa \rightarrow \infty$, $c(q, p) = 0$, the weak formula of Eq. (14) is rewritten as:
 793 Find $\mathbf{u}_h \in V_h, p_h \in Q_h$,

$$\begin{aligned} a(\mathbf{v}_h, \mathbf{u}_h) + b(\mathbf{v}_h, p_h) &= f(\mathbf{v}_h), & \forall \mathbf{v}_h \in V_h \\ b(\mathbf{u}_h, q_h) &= 0, & \forall q_h \in Q_h \end{aligned} \quad (\text{A.1})$$

794 According to the definition of bilinear form b in Eq. (10), for a $\mathbf{u}_h \in \ker \mathcal{P}_h$, then
 795 the second equation of Eq. (A.1) is naturally satisfied. Thus, the above weak
 796 formulation can be equivalently splitted into the following two steps: Firstly, find
 797 $\mathbf{u}_h \in \ker \mathcal{P}_h$,

$$a(\mathbf{v}_h, \mathbf{u}_h) = f(\mathbf{v}_h), \quad \forall \mathbf{v}_h \in \ker \mathcal{P}_h \quad (\text{A.2})$$

798 After determine \mathbf{u}_h , then find $p_h \in Q_h$.

$$b(\mathbf{v}_h, p_h) = f(\mathbf{v}_h) - a(\mathbf{v}_h, \mathbf{u}_h), \quad \forall \mathbf{v}_h \in V_h \quad (\text{A.3})$$

799 To further analyze the error of mixed-formulation, the following properties
 800 of bilinear forms a and b should be defined [63]:

- Continuity:

$$a(\mathbf{v}, \mathbf{u}) \leq C_a \|\mathbf{v}\|_V \|\mathbf{u}\|_V, \quad \forall \mathbf{v}, \mathbf{u} \in V \quad (\text{A.4})$$

$$b(\mathbf{v}, q) \leq C_b \|\mathbf{v}\|_V \|q\|_Q, \quad \forall \mathbf{v} \in V, \forall q \in Q \quad (\text{A.5})$$

- Coercivity:

$$\|\mathbf{v}\|_V \leq \frac{1}{\alpha} \sup_{\mathbf{w} \in V} \frac{|a(\mathbf{v}, \mathbf{w})|}{\|\mathbf{w}\|_V}, \quad \forall \mathbf{v} \in V \quad (\text{A.6})$$

- Inf-sup condition:

$$\|q\|_Q \leq \frac{1}{\beta} \sup_{\mathbf{v} \in V} \frac{|b(\mathbf{v}, q)|}{\|\mathbf{v}\|_V}, \quad \forall q \in Q \quad (\text{A.7})$$

804 where C_a and C_b are positive constants independent of mesh size h . α and β
 805 are the coercivity and inf-sup constants, respectively, which will influence the
 806 accuracy of mixed-formulation.

807 For the error of displacement, the Céa's Theorem used for the error analysis
 808 of traditional Galerkin formulation is not always valid for mixed-formulation.
 809 This is because most of mixed-formulation can not ensure $\ker \mathcal{P}_h \subset \ker \mathcal{P}$ to
 810 maintain the orthogonality of bilinear form a that is required in the proof

of Céa's Theorem. So we first introduce the following error estimator for displacement in the case of $\ker \mathcal{P}_h \not\subset \ker \mathcal{P}$. For any $\mathbf{v}_h \in \ker \mathcal{P}_h$, considering the triangle inequality, the coercivity in Eq. (A.6) and the continuity in Eq. (A.4), we have:

$$\begin{aligned}
\|\mathbf{u} - \mathbf{u}_h\|_V &\leq \|\mathbf{u} - \mathbf{v}_h\|_V + \|\mathbf{v}_h - \mathbf{u}_h\|_V \\
&\leq \|\mathbf{u} - \mathbf{v}_h\|_V + \frac{1}{\alpha} \sup_{\mathbf{w}_h \in \ker \mathcal{P}_h} \frac{|a(\mathbf{v}_h - \mathbf{u}_h, \mathbf{w}_h)|}{\|\mathbf{w}_h\|_V} \\
&\leq \|\mathbf{u} - \mathbf{v}_h\|_V + \frac{1}{\alpha} \sup_{\mathbf{w}_h \in \ker \mathcal{P}_h} \frac{|a(\mathbf{v}_h - \mathbf{u}, \mathbf{w}_h)| + |a(\mathbf{u} - \mathbf{u}_h, \mathbf{w}_h)|}{\|\mathbf{w}_h\|_V} \quad (\text{A.8}) \\
&\leq (1 + \frac{C}{\alpha}) \|\mathbf{u} - \mathbf{v}_h\|_V + \frac{1}{\alpha} \sup_{\mathbf{w}_h \in \ker \mathcal{P}_h} \frac{|a(\mathbf{u} - \mathbf{u}_h, \mathbf{w}_h)|}{\|\mathbf{w}_h\|_V}
\end{aligned}$$

According to Eqs. (A.2), (A.3) and continuity in Eq. (A.5), the second term on the right hand side of above equation can be rewritten as:

$$\begin{aligned}
\sup_{\mathbf{w}_h \in \ker \mathcal{P}_h} \frac{|a(\mathbf{u} - \mathbf{u}_h, \mathbf{w}_h)|}{\|\mathbf{w}_h\|_V} &= \sup_{\mathbf{w}_h \in \ker \mathcal{P}_h} \frac{|a(\mathbf{u}, \mathbf{w}_h) - f(\mathbf{w}_h)|}{\|\mathbf{w}_h\|_V} \\
&= \sup_{\mathbf{w}_h \in \ker \mathcal{P}_h} \frac{|b(\mathbf{w}_h, p)|}{\|\mathbf{w}_h\|_V} \quad (\text{A.9}) \\
&= \sup_{\mathbf{w}_h \in \ker \mathcal{P}_h} \frac{|b(\mathbf{w}_h, p - q_h)|}{\|\mathbf{w}_h\|_V} \\
&\leq C_b \|p - q_h\|_Q
\end{aligned}$$

where q_h is an arbitrary variable in Q_h . Combining the Eqs. (A.8) and (A.9), the following error estimator for displacement can be obtained:

$$\|\mathbf{u} - \mathbf{u}_h\|_V \leq (1 + \frac{C_a}{\alpha}) \inf_{\mathbf{v}_h \in \ker \mathcal{P}_h} \|\mathbf{u} - \mathbf{v}_h\|_V + \frac{C_b}{\alpha} \inf_{q_h \in Q_h} \|p - q_h\|_Q \quad (\text{A.10})$$

Furthermore, for the error estimator of pressure, according to the first equation of Eq. (6) and $V_h \subset V$, we have:

$$b(\mathbf{v}_h, p) = f(\mathbf{v}_h) - a(\mathbf{v}_h, \mathbf{u}), \quad \forall \mathbf{v}_h \in V_h \quad (\text{A.11})$$

and then subtracting Eq. (A.11) from Eq. (A.3) yields:

$$b(\mathbf{v}_h, p - p_h) = -a(\mathbf{v}_h, \mathbf{u} - \mathbf{u}_h), \quad \forall \mathbf{v}_h \in V_h \quad (\text{A.12})$$

822 In this context, for any $q_h \in Q_h$, invoking the triangle inequality, Eqs. (A.7)
823 and (A.5) leads to:

$$\begin{aligned} \|p - p_h\|_Q &\leq \|p - q_h\|_Q + \|q_h - p_h\|_Q \\ &\leq \|p - q_h\|_Q + \frac{1}{\beta} \sup_{\mathbf{v} \in V_h} \frac{|b(\mathbf{v}_h, q_h - p_h)|}{\|\mathbf{v}_h\|_V} \\ &\leq \|p - q_h\|_Q + \frac{1}{\beta} \sup_{\mathbf{v} \in V_h} \frac{|a(\mathbf{v}_h, \mathbf{u} - \mathbf{u}_h)| + |b(\mathbf{v}_h, p - q_h)|}{\|\mathbf{v}_h\|_V} \quad (\text{A.13}) \\ &\leq \frac{C_a}{\beta} \|\mathbf{u} - \mathbf{u}_h\|_V + (1 + \frac{C_b}{\beta}) \|p - q_h\|_Q \end{aligned}$$

824 Consequently, the error estimator for pressure can be given by:

$$\|p - p_h\|_Q \leq \frac{C_a}{\beta} \|\mathbf{u} - \mathbf{u}_h\|_V + (1 + \frac{C_b}{\beta}) \inf_{q_h \in Q_h} \|p - q_h\|_Q \quad (\text{A.14})$$

825 Obviously, the error estimators of Eqs. (A.10) and (A.14) are both related
826 to the coercivity constant α , inf-sup constant β and the approximability of
827 spaces $\ker \mathcal{P}_h$, Q_h , in which the approximability is usually measured by the
828 interpolation error of approximation method. However, the approximability
829 of space $\ker \mathcal{P}_h$ is not trivial to be evaluated directly. To further evaluate the
830 approximability of space $\ker \mathcal{P}_h$, let a variable $\mathbf{w}_h \in V_h \setminus \ker \mathcal{P}_h$ to satisfy the
831 following relationship:

$$\inf_{\bar{\mathbf{v}}_h \in \ker \mathcal{P}_h} \|\mathbf{u} - (\bar{\mathbf{v}}_h + \mathbf{w}_h)\|_V = \inf_{\mathbf{v}_h \in V_h} \|\mathbf{u} - \mathbf{v}_h\|_V \quad (\text{A.15})$$

832 such that the approximability of space $\ker \mathcal{P}_h$ can be transformed to that of
833 space V_h that is easy to be measured. If $\mathbf{w}_h = \mathbf{0}$, $\ker \mathcal{P}_h$ has the identical
834 approximability with V_h :

$$\inf_{\bar{\mathbf{v}}_h \in \ker \mathcal{P}_h} \|\mathbf{u} - \bar{\mathbf{v}}_h\|_V = \inf_{\mathbf{v}_h \in V_h} \|\mathbf{u} - \mathbf{v}_h\|_V \quad (\text{A.16})$$

835 If $\mathbf{w}_h \neq \mathbf{0}$, leading a triangle inequality we have:

$$\|\mathbf{u} - \bar{\mathbf{v}}_h\|_V \leq \|\mathbf{u} - (\bar{\mathbf{v}}_h + \mathbf{w}_h)\|_V + \|\mathbf{w}_h\|_V \quad (\text{A.17})$$

836 where, reconsidering the Eq. (26) in Lemma 1, as $\mathbf{w}_h \in V_h \setminus \ker \mathcal{P}_h$ and $\mathbf{w}_h \neq \mathbf{0}$,
837 the following relation can be obtained:

$$\|\mathbf{w}_h\|_V \leq \frac{1}{\beta} \|\mathcal{P}_h \mathbf{w}_h\|_Q \quad (\text{A.18})$$

838 where, using Eqs. (25), (17) and considering $\mathbf{u} \in \ker \mathcal{P}$, $\bar{\mathbf{v}}_h \in \ker \mathcal{P}_h$, the right
 839 hand side of above equation can further be transformed as follows:

$$\begin{aligned}\|\mathcal{P}_h \mathbf{w}_h\|_Q &= \sup_{q_h \in Q_h} \frac{|\frac{1}{\kappa}(\mathcal{P}_h \mathbf{w}_h, q_h)|}{\|q_h\|_Q} = \sup_{q_h \in Q_h} \frac{|b(\mathbf{w}_h, q_h)|}{\|q_h\|_Q} \\ &= \sup_{q_h \in Q_h} \frac{|b(\mathbf{u} - (\mathbf{w}_h + \bar{\mathbf{v}}_h), q_h)|}{\|q_h\|_Q} \\ &\leq C_b \|\mathbf{u} - (\mathbf{w}_h + \bar{\mathbf{v}}_h)\|_V\end{aligned}\tag{A.19}$$

840 With the combination of Eqs. (A.17), (A.18) and (A.19), the approximability
 841 of $\ker \mathcal{P}_h$ for the case of $\mathbf{w}_h \neq \mathbf{0}$ is given by:

$$\inf_{\bar{\mathbf{v}}_h \in \ker \mathcal{P}_h} \|\mathbf{u} - \bar{\mathbf{v}}_h\|_V \leq (1 + \frac{C_b}{\beta}) \inf_{\mathbf{v}_h \in V_h} \|\mathbf{u} - \mathbf{v}_h\|_V\tag{A.20}$$